



**Universidad  
Zaragoza**

## Trabajo Fin de Máster

# Development of nanostructured titanosilicate catalyst layers in monoliths

Autor

**Diego Sanz Carrillo**

Director

**Reyes Mallada Viana**

Universidad de Zaragoza  
Facultad de Ciencias  
Departamento de Ingeniería Química y Tecnologías del Medio Ambiente  
Instituto de Nanociencia de Aragón

2014

A scientist is happy, not in resting on his attainments  
but in the steady acquisition of fresh knowledge.

*Max Planck*



## ACKNOWLEDGEMENTS

First and foremost, I would like to thank the *Institute of Nanoscience of Aragón* and the SAMCA Foundation for their trust and financial support through the corresponding research and scholarship grants.

I would also like to thank Reyes Mallada, for her tutelage, and Pilar Cea, for her patience and always being willing to help with the Master's issues and paperwork.

I appreciate the help and support provided by all of INAs researchers, specially Ángela and Adrián for their valuable help with this project, and Alberto, for being a stalwart defender of order around the workbench, my first "residence" in the lab. I also appreciate César Rubio's assistance with the JDF-L1 synthesis.

Not less important than the previous acknowledgements, because they helped me keep a good state of mind during the course, was the kindness and friendship of my Master colleagues, autochthonous and foreign alike.

Finally, and on a more personal note, I'll thank my parents for their unconditional support. My thanks to my friends from the University for keeping me in a good mood during the degree and afterwards. My thanks to the "Vacallerows" for bringing a continuous stream of chaos into my life. Also thanks to Jesús, a.k.a. Chico Bellota, for helping me through Module 7 with his logos, and through life with a joke always at hand or an infinite amount of chatter. And last, but not least, to Estela, for her patience during the writing of this report, for enduring my personality and awfully bad jokes during the last five years and counting, and for being awesome altogether.



## TABLE OF CONTENTS

1.- Abstract .....	1
2.- Objectives.....	2
3.- State of the art.....	2
3.1.- Metallic supported catalysts .....	2
3.2.- Titanosilicates as catalyst supports .....	2
3.2.1.- ETS-10.....	3
3.2.2.- JDF-L1 .....	4
3.3.- Structured microreactors .....	5
3.4.- Selective CO oxidation (SELOX).....	6
3.5.- Ethylene epoxidation.....	7
4.- Experimental .....	9
4.1.- Synthesis of catalytic powders.....	9
4.1.1.- Synthesis of titanosilicate supports .....	9
4.1.2.- Synthesis of CoPt <sub>3</sub> nanoparticles .....	11
4.1.3.- Active phase deposition on the supports .....	12
4.2.- Development of structured catalytic microreactors .....	13
4.2.1.- Ceramic monoliths .....	13
4.2.2.- Seeding procedures .....	14
4.2.3.- Growth of support layer by hydrothermal synthesis .....	15
4.2.4.- Active phase deposition on the microreactor.....	17
4.3.- Experimental setups for testing catalytic activity .....	18
4.3.1.- Selective CO oxidation (SELOX).....	18
4.3.2.- Ethylene epoxidation .....	20
4.4.- Characterization techniques.....	21
4.4.1.- Zeta potential .....	21
4.4.2.- Scanning Electron Microscopy (SEM) and Energy-dispersive X-ray Spectroscopy (EDX) .....	22
4.4.3.- Transmission Electron Microscopy (TEM).....	23
4.4.4.- X-ray Diffraction (XRD).....	23
4.4.5.- Microwave Plasma Atomic Emission Spectroscopy (MP-AES) .....	23
4.4.6.- Thermogravimetric Analysis (TGA).....	24
5.- Results and discussion .....	25
5.1.- Catalytic powders.....	25
5.1.1.- Titanosilicate supports characterization .....	25
5.1.2.- CoPt <sub>3</sub> nanoparticles characterization.....	30
5.1.3.- Catalytic powder characterization.....	33
5.2.- Structured catalytic microreactors .....	34
5.2.1.- Seeding of cordierite monoliths .....	34
5.2.2.- Titanosilicate growth on cordierite monoliths .....	36
5.2.3.- Active phase deposition in titanosilicate layers in monoliths.....	40
5.3.- Catalytic activity testing.....	41
5.3.1.- Selective CO oxidation (SELOX).....	41
5.3.2.- Ethylene epoxidation.....	46
6.- Conclusions and future work.....	48
7.- References .....	49



## 1.- Abstract

Supported heterogeneous catalysts are an essential part of the chemical industry, and new supports or catalysts are always under research. Titanosilicates, microporous zeotype materials, are being widely investigated for catalytic support purposes. Structured microreactors, with a high surface to volume ratio and enhanced mass and heat transfer, overcome some of the limitations of fixed bed reactors. Taking into account these considerations, we proposed developing a reproducible method of synthesizing titanosilicate support layers on the channels of ceramic monoliths, for their use in catalysis.

High purity crystals of two different titanosilicate phases (ETS-10 and JDF-L1) were synthesized. These crystals were used for seeding the ceramic monoliths by different methods, of which dip coating and sonication offered the most homogeneous results. Only ETS-10 could be deposited successfully; JDF-L1 crystals were too large. After the seeding, several hydrothermal synthesis methods were tested for the layer growth. The  $\text{TiCl}_3\text{-A}$  method was the most reproducible and offered the most uniform layers. The grown crystal phase was not ETS-10, as the seeds, but JDF-L1, as confirmed by XRD. Catalytic powders of both titanosilicates were prepared by ion exchange or impregnation procedures for their testing in two catalytic reactions: Ethylene Epoxidation and Selective CO Oxidation (SELOX).

For ethylene epoxidation, silver-based powders were prepared. The size of the silver particles obtained in these powders was generally too small for presenting catalytic activity and the catalyst testing provided very poor results or no activity whatsoever.

For SELOX, platinum-based and  $\text{CoPt}_3$  nanoparticle-based powders were prepared, which offered overall very good catalytic activity and reaching total CO conversion, with  $\text{CoPt}_3$  providing better results than Pt as the active phase. Supporting the catalyst on the monolith caused an enhancement of the catalytic performance, and Pt-based monoliths provided slightly better performance than  $\text{CoPt}_3$  powders.



## 2.- Objectives

The main goal of this final master project is to develop a reproducible method for synthesizing ETS-10 and JDF-L1 structured layers well anchored to the walls of monolith microreactors. Furthermore, these layers, after deposition of an active phase, will be tested in catalytic reactions such as CO selective oxidation, or ethylene epoxidation, this last reaction requiring a basic support for better performance.

The main tasks to be accomplished during the project will be:

-Hydrothermal synthesis by secondary growth method of ETS-10 and JDF-L1 on monolithic supports.

-Deposition of silver and platinum, by conventional impregnation and ion exchange methods, on powdered titanosilicates and titanosilicate layers grown on monoliths.

-Characterization of the prepared materials by SEM, TEM, XRD, EDX, MP-AES as well as catalytic test evaluations in experimental setups for each reaction.

## 3.- State of the art

### *3.1.- Metallic supported catalysts*

In the chemical industry, most reactions happen at the surface of an heterogeneous catalyst. Its efficiency will be defined by the quality of the materials used, the exposed surface area of the active phase and its stability. The smaller the size of the active phase particles, the higher the surface area, but too small particles cannot be used in reactors. That's when catalyst supports enter the game. These supports are usually porous materials that allow the highest loading of highly dispersed metal particles possible. The active phase can then be synthesized in the smallest particle size available if needed<sup>[1]</sup>. Several procedures exist for attaching the active phase to the support, but that will not be covered here as some of them are explained in the experimental section 4.1.3.-.

### *3.2.- Titanosilicates as catalyst supports*

Microporous materials such as zeolites and zeotypes present a high surface area and are well known as sorbents and catalytic supports for dispersion of nanoparticles. However, most zeolitic materials present acid sites which promote combustion and should be avoided in selective oxidations, and only a few of these materials possess basic sites. In particular, titanosilicates, such as ETS-10, are characterized for a high basicity and they have been successfully tested in biodiesel production<sup>[2]</sup>. JDF-L1 is another titanosilicate closely related to ETS-10 in composition, but with a layered structure. It has been used

in membranes and other applications, usually after its delamination. The basicity of these titanasilicates can be of use when using them as catalyst supports for reactions like ethylene epoxidation, where the undesired combustion of ethylene oxide to CO<sub>2</sub> is sensitive to the acidity of the catalyst support. If using a basic support, the loss of product and amount of CO<sub>2</sub> generated can be reduced.

### 3.2.1.- ETS-10

The ETS family of microporous titanasilicates discovered in 1989 has a certain degree of disorder in their structure, which supposed a difficulty for solving it. For ETS-10, of empirical formula Na<sub>2-x</sub>K<sub>x</sub>Si<sub>5</sub>TiO<sub>13</sub>·3.5H<sub>2</sub>O, the structure was proposed in 1994<sup>[3]</sup>. A refined framework structure was later obtained which was consistent with the previously proposed model<sup>[4]</sup>. Unlike traditional aluminosilicates or titanasilicates in which Al and Ti atoms are four-coordinated, ETS-10 comprises corner-sharing SiO<sub>4</sub> tetrahedra and TiO<sub>6</sub> octahedra linked through oxygen atoms, forming a three-dimensional 12-membered ring network with a pore-opening size of about 0.8 nm. Each tetravalent Ti atom in an octahedron generates two negative charges, which are balanced by non-framework and exchangeable Na<sup>+</sup> and K<sup>+</sup> cations. These extra framework cations are found in two possible positions, one with a complete coordination sphere of eight O atoms, the other with five O atoms coordinated on one side, which suggests the presence of space filling molecules such as H<sub>2</sub>O to complete the coordination sphere<sup>[4,5]</sup>.

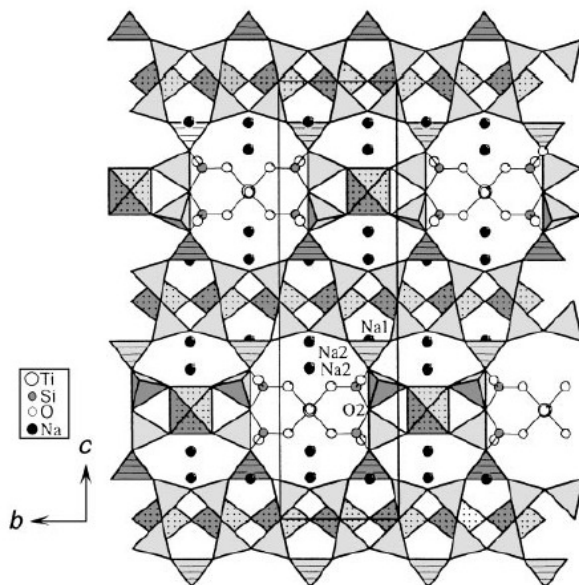
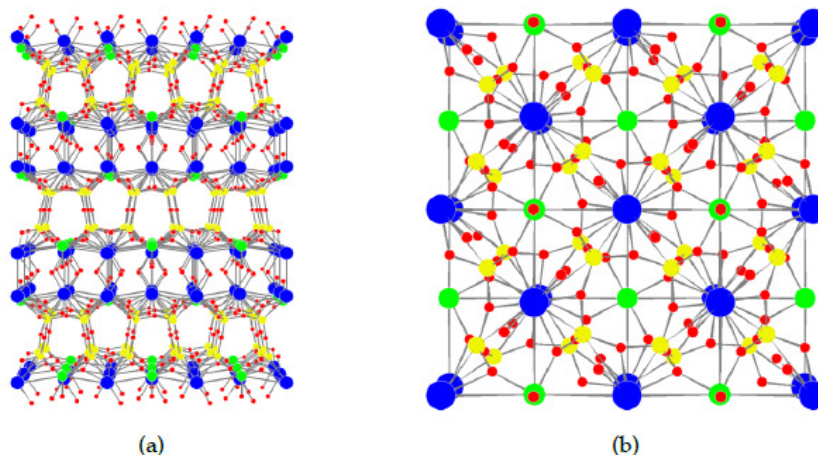


Figure 1.- Projection of the ETS-10 structure down the (100) direction. SiO<sub>4</sub> units are striped or shaded (two types of connections), and TiO<sub>6</sub> units are dotted.

Owing to the high framework charge associated with the octahedral Ti, ETS-10 exhibits a very high cation-exchange capacity which makes it a good ion-exchanger. This very useful behaviour has been proven for certain applications<sup>[6]</sup> and it's a fundamental property for its use as a catalytic support, for the inclusion or deposition of active metals. ETS-10 has also been found to be an excellent catalyst support material in terms of its basicity, which has been assessed by catalytic test using probe reactions such as isopropanol conversion producing acetone and propene. Base-catalyzed dehydrogenation yields acetone, so the selectivity towards this reaction, opposed to acid-catalyzed dehydration forming propene, relates to the catalyst basicity<sup>[7]</sup>.

### 3.2.2.- JDF-L1

JDF-L1 is a layered titanosilicate of empirical formula  $\text{Na}_4\text{Ti}_2\text{Si}_8\text{O}_{22}\cdot 4\text{H}_2\text{O}$  which has a non-centrosymmetric tetragonal structure (P4<sub>2</sub>1<sub>2</sub>). Its structure was established in 1996<sup>[8]</sup> and refined some time later<sup>[9]</sup>. It comprises five-coordinated Ti (IV) ions in the form of  $\text{TiO}_5$  square pyramids linked to  $\text{SiO}_4$  tetrahedra to form continuous sheets. Between each sheet there is a layer of water molecules sandwiched by two layers of exchangeable interlamellar  $\text{Na}^+$  ions to compensate the structure's negative charge. The sheets or layers have five-membered rings (four  $\text{SiO}_4$  tetrahedra and one  $\text{TiO}_5$  pyramid) in the equivalent crystallographic directions [100] and [010]. Along the crystallographic direction [001], sheets are formed by six-membered rings made of two  $\text{TiO}_5$  and four  $\text{SiO}_4$  units. Each of these 6-membered rings are occupied by a  $\text{Na}^+$  cation coordinated with two water molecules<sup>[10]</sup>. A representation of the titanosilicate structure can be seen in *Figure 2*.



**Figure 2.- JDF-L1 representations made with PowderCell 2.4 from crystallographic data (taken from <sup>[10]</sup>). Red: O, Blue: Na, Green: Ti, Yellow: Si. (a) structure's view along [100] or the equivalent [010] direction; (b) view along [001] direction.**

The structure allows pillaring and intercalation with bigger molecules which gives rise to certain applications of the titanosilicate such as catalyst support or ion exchanger<sup>[9]</sup>.

### 3.3.- Structured microreactors

Structured microreactors with channels in the millimeter range have many advantages for its implementation in catalytic applications compared to traditional fixed bed reactors with powder or pellet catalysts. Firstly, the **pressure drop is low**, and they also offer a **high surface to volume ratio** giving rise to **higher heat and mass transfer rates**. One of the main challenges in these structured reactors is the deposition of a stable and highly accessible catalyst layer on the reactor channels or walls.

**Monolith reactors** are the most common form of structured microreactors used in environmental applications. The most widely used procedure for preparing ceramic monoliths is **extrusion**. Monolithic catalysts can be divided into two groups: “**Coated-type**” catalysts (the monolith is an inert ceramic substrate of low surface area, coated with an already made catalyst or a thin film of porous material over which the active phase will be dispersed); “**Incorporated**” catalysts (the active phase is impregnated on a high surface area monolith or included in the monolith composition before it is extruded). The difference between both types is that the active phase is only on the external face of the monolith walls or in all of its structure, respectively<sup>[11]</sup>.

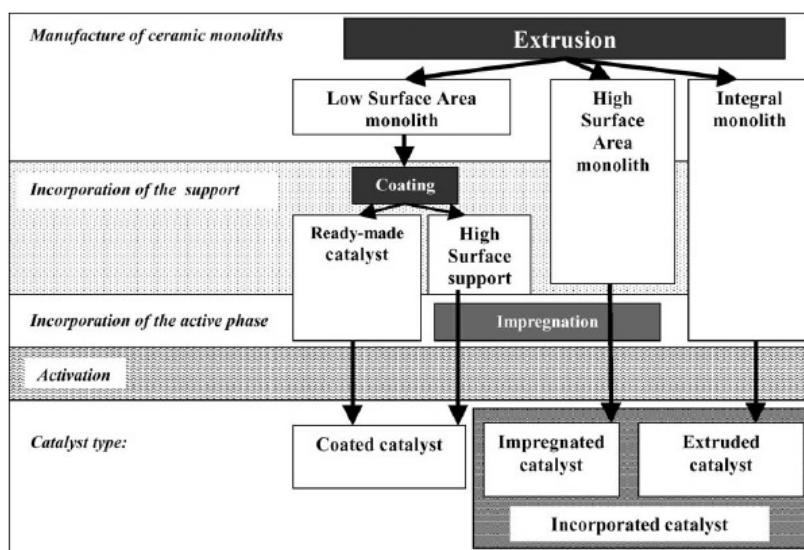


Figure 3.- Diagram of preparation pathways for monolithic catalysts<sup>[11]</sup>.

**Examples of applications** (mainly environmental) for which the use of ceramic monoliths has been reported are: three-way catalysts; ozone abatement in aircraft; CO and HC oxidation in engines; selective reduction of NOx; destruction of volatile organic

compounds (VOC); preferential oxidation of CO (PROX); steam reforming of HCs; hydrogen generation or purification for fuel cells...

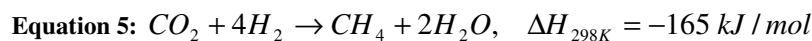
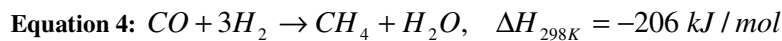
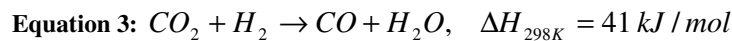
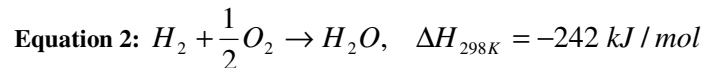
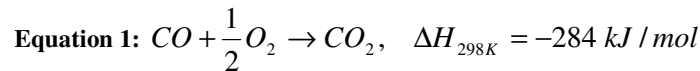
**For our work, we use “coated-type” monolith catalysts as our structured microreactor choice because the “incorporated” ones suppose a higher cost in active noble metals and the accessibility of the reagents is either way limited to a small, outer fraction of wall surface.**

### ***3.4.- Selective CO oxidation (SELOX)***

The main interest for the *selective oxidation of CO (SELOX)* (also known as preferential CO oxidation or *PROX*) relies on the purification of H<sub>2</sub> streams for their use in *Polymer Electrolyte Membrane Fuel Cells (PEMFC)*.

Fuel cells are an efficient and clean mechanism for energy conversion, due to their one-step process (chemical to electrical energy) compared to the several steps involved in combustion based energy systems. Fuel cells provide several more advantages over other systems, and PEMFCs are one of the most promising types of fuel cells, already in early commercialization stage. This and more details about how PEMFCs function can be found elsewhere<sup>[12]</sup>. What is of interest to us is that the Pt-coated anodes used in these fuel cells are easily poisoned by strong chemisorption of carbon monoxide. This makes H<sub>2</sub> streams from reformers unsuitable for feeding cells, since they contain CO coming from several of the fuel reforming reactions. Water gas shift reactors, usually employed for reducing CO concentration in these streams, are not enough for decreasing CO levels below 10 ppm, which is the threshold value the fuel cells can endure. CO-resistant catalysts are being investigated, but selective CO oxidation is the most promising and lowest cost approach to this problem available<sup>[13]</sup>.

In addition to the SELOX reaction (*Equation 1*), several side reactions can happen in the process, such as the water gas shift reaction (*Equation 3*) or methanation reactions:



Hydrogen burning is inevitable once high temperatures have been reached, thus the effort of developing catalysts with a high CO<sub>2</sub> selectivity plus a good enough activity at low temperatures to diminish the loss of hydrogen.

Catalytic activities of several successful metallic catalysts have been reported. Metal oxide catalysts such as Cu/CuO, Ag/Ag<sub>2</sub>O or cerium have been applied in PROX systems. The better performance of a 3d transition metal catalyst was reported for CoO which also showed activity for the reaction as supported CoO catalysts. Supported Au catalysts have shown a very good activity at really low temperatures, though their CO oxidation selectivity decreases rapidly with reaction temperature<sup>[14]</sup>. Platinum group metals (Pt, Pd, Rh, Ru) are also regarded as good catalysts for this application, reaching 100% CO conversion and 30-50% selectivity towards CO<sub>2</sub> production in the range of 150-250 °C. These noble metals are usually supported on alumina, but they have also been tested on different zeolitic supports<sup>[13,14]</sup>.

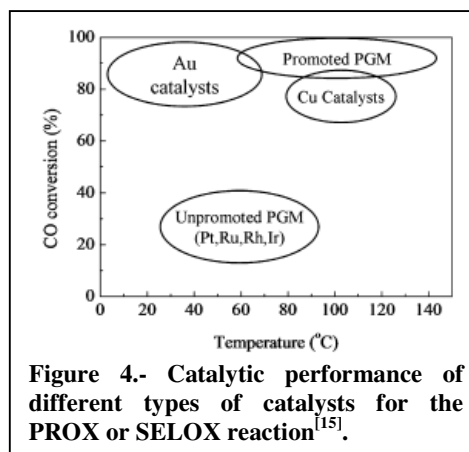


Figure 4.- Catalytic performance of different types of catalysts for the PROX or SELOX reaction<sup>[15]</sup>.

Finally, bimetallic Pt-group-based catalysts have been proven to have better catalytic performances than related monometallic catalysts<sup>[15]</sup>, and among those, Pt-Co intermetallic compounds such as Pt<sub>3</sub>Co seem like promising catalysts for PROX under excess hydrogen<sup>[16]</sup>.

### 3.5.- Ethylene epoxidation

Partial oxidation of ethylene to ethylene oxide (EO) is an important industrial process. So far, silver catalysts are the only ones efficient enough for ethylene epoxidation, since other transition metal catalysts give complete combustion of ethylene due to the ease of CH activation<sup>[17]</sup>, and bibliography on other promising catalysts is seldom found. Unpromoted metallic silver yields only a 50% EO selectivity. The industrial catalysts consist of silver particles supported on low surface area alumina ( $\alpha$ -Al<sub>2</sub>O<sub>3</sub>) and some alkali compound promoters, with ppm amounts of chlorine added to the feed stream also as a promoter to increase EO selectivity. This industrial catalyst has ~90% selectivity, but in terms of the reaction yield there is still room for improvement.

Studies first showed that there were two parallel reactions of the ethylene epoxidation mechanism (Figure 5), selective (k1) and non-selective (k2), that were catalyzed by

silver and happened through an oxometallacycle intermediate (OMC). The OMC forms on the catalyst surface after a reaction between surface adsorbed atomic oxygen and ethylene. The relative barriers of product formation dictate which of them (EO or acetaldehyde [AA]) forms when the OMC dissociates and thus the selectivity. The complete combustions of ethylene or the products are thermodynamically favored (very exothermic processes) but the possibility of selective EO production suggests a kinetically controlled mechanism. These combustions were also found to be sensitive to the acidity of the catalyst support. However, selectivities higher than the supposed maximum (given the lower activation energies of AA for the OMC mechanism) were reported. This incongruence was followed by the proposal of a second reaction channel, a direct epoxidation pathway which would only happen at high oxygen coverage of the catalyst surface. On highly oxygenated Ag surfaces, complex structures known as surface oxides are formed. On these oxides, such as Ag<sub>2</sub>O(001), if there are no vacancies, then no metal atom is available for interaction with ethylene, the OMC complex cannot be stabilized and the surface formation of EO happens through the direct route. This direct formation is enabled by the electrophilic oxygen on the oxide surface, which interacts directly with the C=C double bond forming EO without intermediates<sup>[18]</sup>. Silver is an optimum catalyst for epoxidation, since silver-oxygen interactions lie at point which allows molecular oxygen dissociation, but also moderate binding and activation energies of the products. Silver oxidizes easily at room temperature and is not stable at high temperatures, but these weak Ag-O bonds also increase the epoxidation activity<sup>[17,18]</sup>.



**Figure 5.- Molecular mechanism for ethylene epoxidation through the OMC intermediate.**

For a good performance and EO selectivity, the direct mechanism must be preferred over the OMC intermediate mechanism. For achieving this, oxidation treatments of the catalysts for developing surface oxides on the silver particles can be performed. Additionally, the use of a support with basic sites limits the otherwise favorable ethylene oxide combustion.

## 4.- Experimental

### 4.1.- Synthesis of catalytic powders

This section will cover all procedures conducted during the experimental work of the project leading towards obtaining titanasilicate-based catalytic powders. As a first step, small crystals of the selected titanosilicates must be synthesized. The next step involves the deposition of the metallic active phase on the catalytic support. These metals are *silver for ethylene epoxidation* and *platinum for selective CO oxidation*, and can be deposited on the supports by several methods, being *Ion Exchange* and *Incipient Wetness Impregnation* the ones explored in this work. *CoPt<sub>3</sub> nanoparticles* were also synthesized and deposited on the supports by means of *electrostatic stabilization* for their use in selective CO oxidation.

#### 4.1.1.- Synthesis of titanasilicate supports

##### Synthesis of ETS-10

Crystals of the titanasilicate ETS-10 were obtained following a *hydrothermal synthesis procedure* based on the previous works of Rocha et al.<sup>[19]</sup> and various members of the Nanoporous Films and Particles group of the Nanoscience Institute of Aragón<sup>[20]</sup>, using *Anatase (TiO<sub>2</sub>) as the source of Titanium*. To prepare a gel of molar composition **4.8 Na<sub>2</sub>O / 1.4 K<sub>2</sub>O / TiO<sub>2</sub> / 5.1 SiO<sub>2</sub> / 125 H<sub>2</sub>O**, deionized water (23.22 g), NaCl (*Merck*) (5.06 g) and KCl (99.0 wt.%, *Panreac*) (1.23 g) were mixed and stirred until complete dissolution of the salts. Afterwards, a sodium silicate solution (10.6 wt.% Na<sub>2</sub>O, 26.5 wt.% SiO<sub>2</sub>, *Sigma-Aldrich*) (17.69 g) was slowly added while increasing the stirring. The solution was kept under stirring for 1h and 30 min. After that time, KF ( $\geq 99.0$  wt.%, *Sigma-Aldrich*) (1.57 g) was added and the solution was stirred for an additional 20 min. Finally, TiO<sub>2</sub> (Anatase, <25 nm nanopowder, 99.7 wt.%, *Sigma-Aldrich*) (1.22 g) was added to the mixture to obtain approximately 50 g of a white gel which was stirred for 1h. The pH of our gel was usually around 10.8. According to Rocha et al.<sup>[19]</sup>, *pH is a critical value for obtaining pure titanasilicate phases*. Based on his results, the optimum pH for obtaining pure ETS-10 would be pH = 10.4 ± 0.2. Thus, the pH of the gel was measured (*Cyberscan pH 2100, Eutech Instruments; Hamilton Filltrode* probe with *Skylyte-CL* electrolyte) and adjusted using concentrated HCl (37 wt.%, *Sigma-Aldrich*) to minimize the increase on the molar ratio of water.



After pH adjustment, the gel was transferred to a 35 mL Teflon-lined autoclave and kept 24h in an oven at 230 °C for the static crystallization to take place. After that time, the autoclave was quenched using tap water. The contents of the autoclave were then centrifuged (10000 rpm, 10 min; *Heraeus MEGAFUGE 16R Centrifuge, Thermo Scientific*) and washed with deionized water several times. The recovered solid was then dried overnight at 110 °C, finally obtaining ca. 5 g of powder.

### **Synthesis of JDF-L1**

Crystals of JDF-L1 were synthesized by *unseeded hydrothermal synthesis* following the procedure developed by Rubio et al.<sup>[10,21]</sup> using  $\text{TiCl}_3$  as Ti source. To prepare a gel of molar composition **2.9 Na<sub>2</sub>O / TiO<sub>2</sub> / 4.2 SiO<sub>2</sub> / 101 H<sub>2</sub>O**, a sodium silicate solution (8 wt.% Na<sub>2</sub>O, 27 wt.% SiO<sub>2</sub>, *Merck*) (10.05 g) was mixed with deionized water (6.54 g) and NaOH ( $\geq 98$  wt.%, pellets, *Sigma-Aldrich*). After adding the  $\text{TiCl}_3$  solution (20% wt.% in 3 wt.% HCl, *Alfa Aesar*) (8.24 g), the mixture turned into a bluish-black gel which was almost a dry solid. This gel was stirred manually for 5 min until it started turning into a liquid gel again, and then was kept stirring for 1h. Afterwards, the gel was degassed in an ultrasonic bath (*JP Selecta, Ultrasons* model, 40 kHz), and then transferred to a 35 mL Teflon-lined autoclave where the static crystallization took place for 93h at 230 °C. After that time, the autoclave was quenched with tap water and the solid was filtered (2-3  $\mu\text{m}$  pores, 200  $\mu\text{m}$  thickness; *PRAT DUMAS*), washed several times with deionized water and dried overnight at 110 °C. About 3.8 g of powder were obtained.

Crystals of JDF-L1 were also obtained by *seeded hydrothermal synthesis*. The procedure used was exactly the same as for the unseeded synthesis, but adding 79 mg of the crystals from the previous synthesis (thoroughly grounded) to the new synthesis gel, which was kept in the oven for only 24h. Circa 4.2 g of powder were obtained.

*As with the synthesis of other titanosilicates, pH is a critical factor, however no adjustment of pH was necessary since the amount of reagents is optimized for obtaining a gel with a pH value around 10.4. However, this can be checked by 1/100 dilution of a fraction of the gel to measure its pH (dilution needed for an adequate contact with the pH-meter probe).*

A brief summary of the most relevant information of both titanosilicate syntheses is collected in *Table 1*.

**Table 1.- Summary of methods for obtaining small crystals of ETS-10 and JDF-L1 by hydrothermal synthesis. For all methods: pH 10.4; Static crystallization; T=230 °C.**

Method name	Molar ratio of the synthesis gel	Seeding	Synthesis time
ETS-10 TiO <sub>2</sub>	4,8 Na <sub>2</sub> O / 1,2 K <sub>2</sub> O / TiO <sub>2</sub> / 5,1 SiO <sub>2</sub> / 125 H <sub>2</sub> O	No	24 h
JDF-L1 TiCl <sub>3</sub>	2,9 Na <sub>2</sub> O / TiO <sub>2</sub> / 4,2 SiO <sub>2</sub> / 101 H <sub>2</sub> O	No	93 h
JDF-L1 TiCl <sub>3</sub> -S	2,9 Na <sub>2</sub> O / TiO <sub>2</sub> / 4,2 SiO <sub>2</sub> / 101 H <sub>2</sub> O	Yes	24 h

The *yield* of these syntheses was calculated with the mass of solids obtained after synthesis and the mass of reagents employed. The mass of solid, along with the molecular weight of the appropriate titanosilicate (**ETS-10**:  $Na_{1,6}K_{0,4}Si_5TiO_{13} \cdot 3,5H_2O$ ,  $MW=511,84$  g/mol; **JDF-L1**:  $Na_4Si_8Ti_2O_{22} \cdot 4H_2O$ ,  $MW=836,60$  g/mol) will give us the experimental moles of titanosilicate obtained. The maximum theoretical moles which could be obtained can be known by the moles of Si or Ti (whichever is the limiting reagent) that were added to the synthesis. Dividing experimental by theoretical moles, the yield of the synthesis is obtained.

#### 4.1.2.- Synthesis of CoPt<sub>3</sub> nanoparticles

Pt-based intermetallic compounds (IMCs) may be promising catalysts for the selective oxidation of CO<sup>[16]</sup> and, in fact, CoPt<sub>3</sub>-ETS-10 catalytic powders have already been tested by a fellow researcher of the NFP group of the Nanoscience Institute of Aragón. All steps required to prepare the bimetallic nanoparticles<sup>[22]</sup> were carried out under N<sub>2</sub> atmosphere and vigorous stirring at 0 °C. Firstly, a NaBH<sub>4</sub> (≥99 wt.%, *Sigma-Aldrich*) ethanol solution (100 mL, 0.066M) was added drop by drop to a CoCl<sub>2</sub> (≥98 wt.%, anhydrous, *Sigma-Aldrich*) ethanol solution (100 mL, 3.6 mM) which also contained 0.5000 g of PVP (M.W.=10000, *Sigma-Aldrich*). The solution suffers a colour change from blue [Co(II)] to brown [Co(0)] indicative of the formation of cobalt nanoparticles. Then, a H<sub>2</sub>PtCl<sub>6</sub> (~38 wt.% Pt, *Sigma-Aldrich*) ethanol solution (100 mL, 10.8 mM) was added drop by drop to the previous nanoparticle suspension. After 30 min of vigorous stirring, another NaBH<sub>4</sub> ethanol solution (100 mL, 0.066M) was slowly added and the mixture was kept under stirring for 3h. Afterwards, the final suspension was subjected to several cycles of centrifugation (12000 rpm, 15 min) and ethanol washing. Previous experiences from other NFP researchers suggested that drying the nanoparticle suspension and redispersing it later when needed caused too much aggregation of the NPs, even after sonication, so the CoPt<sub>3</sub> NPs were kept in ethanol.

### 4.1.3.- Active phase deposition on the supports

*Ion Exchange* is a common procedure in zeolite-like materials, where ions of a certain metal are incorporated into the matrix by exchange in solution with the extra framework cations of said matrix. In the case of ETS-10 and JDF-L1 the extra framework cations are  $\text{Na}^+$  and  $\text{K}^+$ . *Incipient Wetness Impregnation (IWI)* is another common technique for the synthesis of heterogeneous catalysts. A salt containing the metal precursor is dissolved and added to the catalyst support in a quantity approximately equal to the pore volume of this support, so the mass transfer is driven by capillary action and not diffusion (much slower). Both of these deposition techniques require afterwards a *calcination step*, with the dual objective of decomposing (or driving off, if volatile) other remanent chemicals of the solutions, and causing the *annealing* of the metal ions into active metal particles or clusters.

#### **Ionic Exchange (Ag)**

The Ag(I)-exchanged titanosilicate samples were obtained by adding 400 mg of ETS-10 or JDF-L1 to 100 mL of an  $\text{AgNO}_3$  (99.9999 wt.%, *Sigma-Aldrich*) aqueous solution (5.56 mM) and stirring the solution for 24h. Once the ion exchange was finished, the solution was centrifuged and the solid washed with water several times. Afterwards, the powder was dried in a furnace at 100 °C for 5h and then calcined at 500 °C for 1h. The amount of silver used in this procedure is a 15% of the mass of titanosilicate. However, since the ion exchange is a diffusion equilibrium process, such a high loading won't be reached. The experimental metal loading of the titanosilicate crystals will be lower than a 15 wt.% Ag.

#### **Ionic Exchange (Pt)**

A similar procedure is conducted for obtaining Pt(II)-exchanged titanosilicate samples, adding 300 mg of titanosilicate to 100 mL of a  $[\text{Pt}(\text{NH}_3)_4](\text{NO}_3)_2$  (99.995 wt.%, *Sigma-Aldrich*) aqueous solution (0.25 mM) and stirring for 24h, followed by several cycles of centrifugation and washing. Finally, the powder is calcined in a furnace at 350 °C for 3h using a temperature ramp of 2 °C/min. Due to equilibrium process, the experimental metal loading of the crystals will be lower than the theoretical 1.7 wt.% Pt.

#### **Incipient Wetness Impregnation (Ag)**

For this method, 0.5 mL of an  $\text{Ag}(\text{NO}_3)$  aqueous solution (1.11 M) were added to 400 mg of the titanosilicate (*in the case of JDF-L1, with a larger pore volume, 0.5 mL of water were also added*) and the slurry was grounded for around 5-10 min. The slurry

was then dried for 5h at 100 °C and calcined in a furnace at 500 °C for 1h. The expected silver loadings are approximately 15 wt.% Ag.

### **CoPt<sub>3</sub> nanoparticle deposition on the supports**

Nanoparticle deposition on the titanosilicate supports was achieved through electrostatic stabilization, due to the negative superficial charges both the nanoparticles and the supports present in aqueous and ethanolic solutions (see *Figure 18*). As the first step, a polyethyleneimine (PEI) solution is prepared by dissolving 250 mg of PEI (branched, M.W.=25000, *Sigma-Aldrich*) in 20 g of deionized water. This PEI solution (1.4 g) is added to 500 mg of the titanosilicate support and the mixture is sonicated 15 min in an ultrasonic bath and later dried at 100 °C for at least 1h. The suspension of CoPt<sub>3</sub> nanoparticles in ethanol obtained before is added to the PEI-functionalized titanosilicate in a quantity such that the mass of particles is a 3% of the titanosilicate mass. The final loading of particles may be lower. (*The volume of NP suspension needed can be known by drying fractions of it and measuring the solid residue to obtain an approximate concentration*). The mixture is sonicated 15 min in an ultrasonic bath and later dried at 80 °C for 3h. Afterwards, the powder is calcined in a furnace with a heating ramp of 2 °C/min up to 500 °C, which is maintained for 2h.

## ***4.2.- Development of structured catalytic microreactors***

Another of our objectives is developing structured catalytic microreactors and testing them for the same reactions as the corresponding powders. To achieve that we seeded cordierite monoliths, conducted hydrothermal syntheses to create well-intergrown titanosilicate layers on the inner surface of the monoliths and, finally, deposited the active metals onto the support layers.

### **4.2.1.- Ceramic monoliths**

As the structural component of our catalytic microreactors we chose ceramic monoliths. Specifically, monoliths made of *cordierite*, a magnesium-aluminosilicate (2MgO x 2Al<sub>2</sub>O<sub>3</sub> x 5SiO<sub>2</sub>) with a very low thermal expansion coefficient (TEC), high refractoriness and good mechanical strength among other properties<sup>[11]</sup>. The monoliths used in this work, provided by *Corning*, were made of synthetic cordierite and had a cell density of 400 cells/inch<sup>2</sup>. Large monolith pieces were cut down using a utility knife until they had between 1.5 and 2 cm in length and between 1.2 and 1.5 cm in diameter or width. They were cut as square-prisms for all the testing and analysis, except the

monoliths meant for use in the catalytic reaction setups which were cut as cylinders for a better fitting into the quartz tubes used in those setups. For all the seeding, growth and catalyst deposition steps, the monoliths were covered with teflon tape to avoid deposition or growth on their external walls.

#### **4.2.2.- Seeding procedures**

Three different methodologies were considered for depositing small crystals of titanosilicates onto the internal surface of the monoliths.

##### **Sonication**

*This method is based on immersing the pristine monolith into a suspension containing the titanosilicate seeds and then sonicating the suspension in an ultrasonic bath to favor the movement and deposition of the crystals onto the rough surface of the monolith channels, while at the same time preventing crystal sedimentation.*

Two different concentrations of the titanosilicate suspension were tested: ~13 wt.% seeds and ~2.5 wt.% seeds. The monoliths were subjected to 2 immersions, sonicating for 20 min each, blowing with nitrogen the excess of suspension after each immersion. The monoliths were later dried at 110 °C for at least 3h.

##### **Layer by layer deposition by Electrostatic Stabilization (LbL by ES)**

Due to the repulsive nature of the interactions between titanosilicate crystals and cordierite (see Figure 18 in Section 5.1.-), the attachment of an oppositely charged polymer to one of the materials can lead to a better adhesion of the crystal seeds to the monolith surface due to electrostatic stabilization. This process consisting on depositing the polymer and then the seeds can be repeated several times and is known as layer by layer deposition<sup>[23]</sup>. Cordierite, ETS-10 and JDF-L1 have negative surface charges, so a cationic polymer is needed. Polyethyleneimine (PEI) and Poly(diallyldimethylammonium chloride) (PDDA) are two polymers which can be found in literature<sup>[23,24]</sup> being used for these purposes.

The procedure is identical for both polymers. The monolith is first immersed in a 0.4 wt.% aqueous solution of PEI (branched, M.W.=25000, *Sigma-Aldrich*) or PDDA (20 wt.% in H<sub>2</sub>O, M.W.=100000-200000, *Sigma-Aldrich*) and sonicated for 10 min. The polymer is then rinsed in water and air blown. Next, it is immersed in a 2.5 wt.% suspension of the titanosilicate seeds, sonicated for 10 min, rinsed and air blown. This cycle of immersion in polymer solution and seed suspension is repeated once more. Afterwards the monolith is dried in an oven at 110 °C and calcined in a furnace at 550

°C for 3h with a ramp of 2 °C/min, so the polymer is completely eliminated, to avoid its possible interference with the subsequent hydrothermal synthesis.

### **Dip coating**

*Dip coating is a process in which a substrate is immersed in a suspension of the material to be deposited and then it is taken out slowly, at a constant speed, causing its deposition (the final thickness of the deposited layer depends on the withdrawal speed). The substrate is then left to dry, so all the solvent evaporates allowing the formation of a thin film of the deposited material.*

For the deposition of titanosilicate seed crystals onto cordierite monoliths, a home-made dip-coating setup was employed, comprising a peristaltic pump and two wide burettes. The suspension used had a 13 wt.% of seeds and the immersion-withdrawal cycle was repeated 4 times, using a withdrawal speed of 1 cm/min.

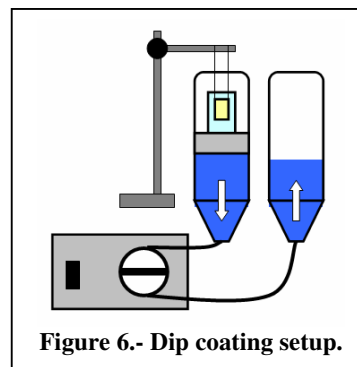


**Figure 6.- Dip coating setup.**

**Table 2.- Main parameters of the different seeding procedures.**

<i>Seeding method</i>	<i>Polymer solution</i>	<i>Immersion</i>	<i>Duration</i>	<i>Seed suspension</i>	<i>Immersion</i>	<i>Duration</i>	<i>Withdraw speed</i>
<b>Sonication (13 wt.%)</b>	-	-	-	~13 wt.%	2	20 min	-
<b>Sonication (2.5 wt.%)</b>	-	-	-	~2.5 wt.%	2	20 min	-
<b>LbL by ES (PEI)</b>	0.4 wt.%	2	10 min	~2.5 wt.%	2	10 min	-
<b>LbL by ES (PDDA)</b>	0.4 wt.%	2	10 min	~2.5 wt.%	2	10 min	-
<b>Dip Coating</b>	-	-	-	~13 wt.%	4	-	1 cm/min

### **4.2.3.- Growth of support layer by hydrothermal synthesis**

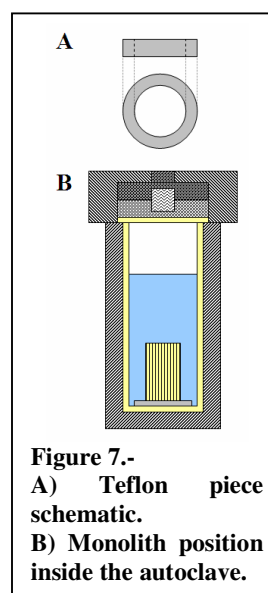
To prepare a continuous titanosilicate layer on the monolith's inner surface, different hydrothermal synthesis gels were tested. These gels, modified from the bibliography<sup>[19,20]</sup>, were initially designed for seeded and/or unseeded synthesis of free ETS-10 crystals using  $TiCl_3$  as the Ti source, with the crystals so obtained being much larger than those from the Anatase route used for seed synthesis in *Section 4.1.1.-*. Due to the size of the synthesized crystals, it is expected that a seeded synthesis with these gels onto a support such as the cordierite monoliths will lead to large crystals of the titanosilicate intergrowing into an homogeneous layer covering the whole internal surface, as previously reported for alumina supports and metallic microreactor channels<sup>[25]</sup>.

The synthesis method referred to as “TiCl<sub>3</sub> A” is explained in detail in the following paragraphs, while the rest of the methods tested have very similar procedures and thus can be extrapolated from the information given in *Table 3*.

#### **“TiCl<sub>3</sub> A” method for titanosilicate layer growth on monoliths**

To prepare a synthesis gel of molar composition 4.2 Na<sub>2</sub>O / 1.2 K<sub>2</sub>O / TiO<sub>2</sub> / 5.6 SiO<sub>2</sub> / 343 H<sub>2</sub>O, TiCl<sub>3</sub> solution (15 wt.% in 5-10 wt.% HCl, *Riedel-de Hën*) (6.5g) was mixed with deionized water (27.5g). Hydrogen peroxide (30 wt.% in H<sub>2</sub>O, *Sigma-Aldrich*) (0.85g) was then added under constant stirring to oxidize Ti(III) into Ti(IV), causing the solution to change colour from violet to red. Then, KCl (99 wt.%, *Panreac*) (1.1g) and NaOH (≥98 wt.%, pellets, *Sigma-Aldrich*) (1.3g) were added and another colour change observed, from red to light orange, at the same time the mixture got denser. The slow addition of a sodium silicate solution (8 wt.% Na<sub>2</sub>O, 27 wt.% SiO<sub>2</sub>, *Merck*) (7.8g) yielded the final gel, which turned from light orange to a light yellow or cream colour. The pH was measured and adjusted to 10.4 ± 0.2.

With the help of a hollow cylindrical teflon piece (*Figure 7 A*) to avoid channel blocking against the bottom of the autoclave, the monolith is introduced vertically into a teflon-lined 35 mL autoclave (*Figure 7 B*), which is then filled to ¾ its capacity with the previously synthesized gel. Hydrothermal synthesis is then conducted by putting the autoclave in an oven at 230 °C for 36h. After the crystallization, the autoclaves are quenched with tap water to stop the synthesis. The monolith is taken out, washed with deionized water, air blown, sonicated in deionized water for 5-10 seconds and then washed and air blown again. It is finally dried at 110 °C.



Due to the limited accessibility of the gel into the monolith, primary nucleation always happens in the bulk of the gel outside the monolith. The gel or solids remaining inside the autoclave after removing the monolith can be recovered (by centrifugation, washing and drying, as specified previously for the ETS-10 seeds) to compare the titanosilicate phases grown inside and outside the monolith.

As previously stated, *Table 3* contains information on all the methods used for the titanosilicate layer growth on monoliths. Each method with a distinctive synthesis gel is given an identificative letter, while methods with small modifications such as the use of a rotatory oven, not using hydrogen peroxide, or different synthesis times, all while

maintaining the same gel molar ratio, are identified with the same letter as the parent method but adding a suffix.

**Table 3.- Summary of the different methodologies tested for the growth of a titanosilicate layer onto the monolith supports. For all methods: Gel pH = 10.4.**

Method name	Synthesis gel		Hydrothermal synthesis conditions		
	Molar ratio	Use of H <sub>2</sub> O <sub>2</sub>	Time	Temperature	Oven
TiCl <sub>3</sub> -A	4.2 Na <sub>2</sub> O / 1.2 K <sub>2</sub> O / TiO <sub>2</sub> / 5.6 SiO <sub>2</sub> / 343 H <sub>2</sub> O	Yes	36 h	230 °C	Static
TiCl <sub>3</sub> -A*		No	72 h		
TiCl <sub>3</sub> -A**		Yes	45 h		
TiCl <sub>3</sub> -A/R		Yes	36 h		
TiCl <sub>3</sub> -B	2.9 Na <sub>2</sub> O / 1.8 K <sub>2</sub> O / TiO <sub>2</sub> / 5.3 SiO <sub>2</sub> / 280 H <sub>2</sub> O	No	72 h	200 °C	Static
TiCl <sub>3</sub> -B*	4.7 Na <sub>2</sub> O / 1.8 K <sub>2</sub> O / TiO <sub>2</sub> / 5.3 SiO <sub>2</sub> / 280 H <sub>2</sub> O				
TiCl <sub>3</sub> -C	4.2 Na <sub>2</sub> O / 1.2 K <sub>2</sub> O / TiO <sub>2</sub> / 5.6 SiO <sub>2</sub> / 202 H <sub>2</sub> O	Yes	36 h	230 °C	Static
TiCl <sub>3</sub> -D	4.6 Na <sub>2</sub> O / 1.5 K <sub>2</sub> O / TiO <sub>2</sub> / 5.2 SiO <sub>2</sub> / 124 H <sub>2</sub> O	Yes	36 h	230 °C	Static
TiCl <sub>3</sub> -E	4.6 Na <sub>2</sub> O / 1.5 K <sub>2</sub> O / TiO <sub>2</sub> / 5.2 SiO <sub>2</sub> / 203 H <sub>2</sub> O	Yes	36 h	230 °C	Static
TiCl <sub>3</sub> -E*			24 h		
TiCl <sub>3</sub> -E/R			36 h		

#### 4.2.4.- Active phase deposition on the microreactor

As with the catalytic powders, the appropriate active phases for our studied reactions can be introduced into the titanosilicate layer by ion exchange, which is followed by a thermal reduction step.

##### Ion Exchange (Ag and Pt)

The Ion Exchange procedure for the titanosilicate layers grown on monoliths is mainly the same as for the titanosilicate crystals. The same reagents, their amount, solution volume, exchange time and calcination procedure are used, for both Ag and Pt exchanges. The only difference is that, instead of suspending the powdered titanosilicate in the solution, a layer grown monolith is immersed in the solution and positioned, with the help of a teflon piece and teflon tape, in such a way that the stirring causes the solution to constantly flow in and outside of the monolith's channels.

The weight of titanosilicate inside the monoliths once the layers have been grown averaged **160 mg** for the TiCl<sub>3</sub>-A method (chosen as the ideal growth method). This means that we had a higher metal precursor/titanosilicate ratio in comparison with the ion exchange procedure for the powders, so higher theoretical loadings were expected.



### 4.3.- Experimental setups for testing catalytic activity

Once obtained and ready, both the catalytic powders and the structured catalyst layer microreactors were ready for their catalytic activity testing on each specific experimental setup.

#### 4.3.1.- Selective CO oxidation (SELOX)

In the SELOX reaction setup, the catalytic powders and microreactors containing Pt or bimetallic CoPt<sub>3</sub> nanoparticles as active components were tested for catalytic activity.

The reactor and experimental setup used for this work are schematized in *Figure 8*. The gas chromatograph was a *CP-4900 Micro GC* from *Varian*, which comprised a MS5A molecular sieve column and a PPQ column with the corresponding TCD detectors, which allow the analysis of permanent gases (O<sub>2</sub>, N<sub>2</sub>, H<sub>2</sub> and CO), and of CO<sub>2</sub> and H<sub>2</sub>O, respectively. Gas cylinders were provided by *Praxair* (H<sub>2</sub>, 99.999 %; O<sub>2</sub>, 99.99%; N<sub>2</sub>, 99.999 %; CO<sub>2</sub>, 99.995 %; H<sub>2</sub>-CO mixture, 1.3 v.% CO with H<sub>2</sub> balance).

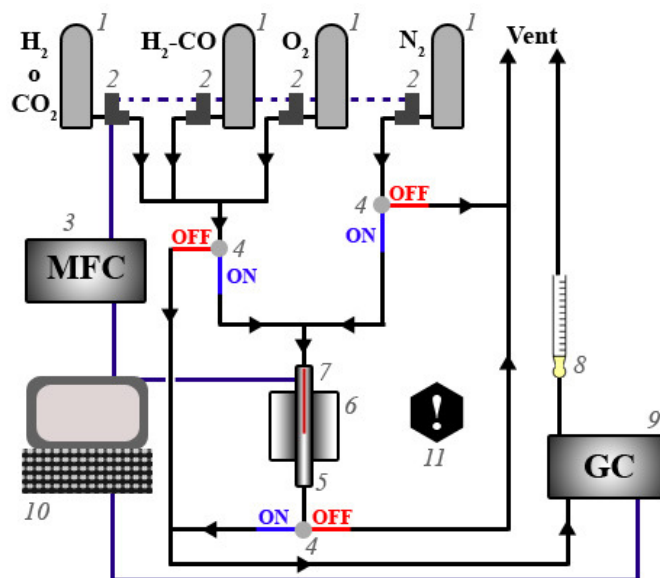


**Figure 8.-** Experimental setup for catalytic activity analysis of SELOX powder and microreactor catalysts. 1- Feed gas cylinders. 2- Mass flow meters (*5850 TR series, Brooks*). 3- Mass flow controller. 4- Valves for operation control. 5- Quartz reactor ( $\phi = 7$  mm for powders or  $\phi = 16$  mm for monoliths). 6- Oven with PID Eurotherm temperature controller. 7- Thermocouple with quartz sheath and temperature controller. 8- Bubble-meter for inlet and outlet flow measurement. 9- Gas chromatographer. 10- Computer system and software. 11- Portable CO sensor.

For the catalytic powder testing, 200 mg of the catalyst were mixed with 300 mg of silica spheres for enhanced heat dissipation. The resulting powder was introduced into the quartz tube reactor at an intermediate height (to ensure isothermal heating from the oven) with the aid of glass wool. The catalyst bed was then compressed a little bit,

carefully knocking the quartz tube or using a steel rod. Once compressed, the thermocouple's sheath was inserted into the bed until it was at half the total height of said catalyst bed.

For the monolith testing, some lines and connections of the setup had to be changed to use the bigger quartz tube. The monolith was rolled with teflon tape until it fit snugly inside the tube and then it was pushed to an intermediate height. If the monolith cannot hold by itself, glass wool can be used as stopper for a better grip. The thermocouple's sheath was placed just above the monolith, in contact with it. The temperature measurement was not as reliable as with the powder catalyst but served as reference.

Before the SELOX process, the catalyst was submitted to an in-situ reduction step carried out by heating the oven to 350 °C (2 °C/min) for 3h, while introducing a gas feed consisting of 20 v.% H<sub>2</sub> and 80 v.% N<sub>2</sub>, with a flow of 70 NmL/min.

The catalytic testing for the SELOX reaction was conducted at different reactor temperatures, ranging from 50 °C to 250 °C. The inlet fed to the reactor had the following gas composition: 74 v.% H<sub>2</sub>, 1 v.% O<sub>2</sub>, 1 v.% CO, 21 v.% CO<sub>2</sub>, ~3 v.% H<sub>2</sub>O. Water was added to the flow of gases by making the feed pass through a bubbler placed just before the access to the reactor (not shown in *Figure 8*).

The parameter  $\lambda$  is defined as the oxygen excess versus the stoichiometric amount required to oxidize all the CO in the feed. For our gas feed  $\lambda=2$  is used, which provides better performance than using stoichiometric quantities of O<sub>2</sub> since the reaction is not 100% selective.

Weight hourly space velocity (WHSV) is defined as the gas flow divided by the amount of catalyst. For the fixed bed reactors, **200 mg** of catalyst and a flow of **100 NmL/min** of feed were used, so **WHSV = 30 mL/h·mg**. For the monolithic microreactors, the amount of catalyst may vary depending on the seeding and growth method the monolith has experienced (averaging **160 mg** for the TiCl<sub>3</sub>-A synthesized layers, the ones finally used). Thus the gas flow had to be adjusted (**80 NmL/min** for TiCl<sub>3</sub>-A monoliths) for the WHSV to be the same and the results of the microreactors comparable with those of the fixed bed reactors.

From the data obtained in the catalytic testing, CO conversion, O<sub>2</sub> conversion and CO<sub>2</sub> selectivity were calculated using the following formulas:

$$\text{Equation 6: CO conversion (\%)} = \frac{[CO]_{in} - [CO]_{out}}{[CO]_{in}} \cdot 100$$

$$\text{Equation 7: } O_2 \text{ conversion (\%)} = \frac{[O_2]_{in} - [O_2]_{out}}{[O_2]_{in}} \cdot 100$$

$$\text{Equation 8: } CO_2 \text{ selectivity (\%)} = 0.5 \cdot \frac{[CO]_{in} - [CO]_{out}}{[O_2]_{in} - [O_2]_{out}} \cdot 100$$

### 4.3.2.- Ethylene epoxidation

In the ethylene epoxidation reaction setup, the catalytic powders containing Ag as catalyst were tested for catalytic activity.

The reactor and experimental setup used for this work are schematized in *Figure 9*. The gas chromatograph was a *490 Micro GC* from *Agilent Technologies*, which comprised 2 M5AH molecular sieve columns, a PPQ column and a 5CB column, with the corresponding TCD detectors. Gas cylinders were provided by *Praxair* (O<sub>2</sub>, 99.99%; C<sub>2</sub>H<sub>4</sub>, 40 v.% with He balance; He, 99.9%).

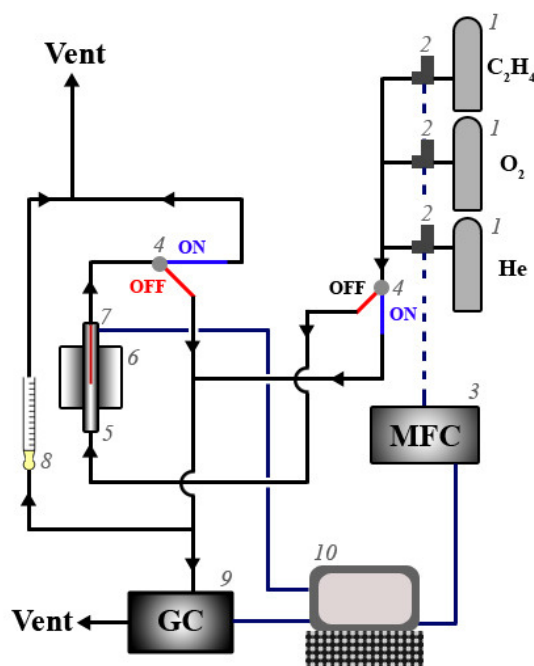


**Figure 9.-** Experimental setup for catalytic activity analysis of ethylene epoxidation catalytic powders. 1- Feed gas cylinders. 2- Mass flow meters (*EL-FLOW Select, Bronkhorst*). 3- Mass flow controller. 4- Valves for operation control. 5- Quartz reactor ( $\phi = 7$  mm). 6- Oven with PID Eurotherm temperature controller. 7- Thermocouple with temperature controller. 8- Bubble-meter for inlet and outlet flow measurement. 9- Gas chromatographer. 10- Computer system and software.

For the catalytic powder testing, 300 mg of the catalyst were introduced into the quartz tube reactor at an intermediate height (to ensure good heating from the oven) with the aid of glass wool. The catalyst bed was then compressed a little bit, carefully knocking

the quartz tube or using a steel rod. Once compressed, the thermocouple was inserted into the bed until it was at half the total height of said catalyst bed.

Before the ethylene epoxidation reaction, the catalyst was submitted to an oxidation step due to the need of silver oxide on the surface of the catalyst particles for a good catalysis performance<sup>[18]</sup>. The oxidation step was carried out by heating the oven to 200 °C (10 °C/min) for 2h, while introducing a gas feed consisting of 20 v.% O<sub>2</sub> and 80 v.% He with a gas flow of 100 NmL/min. The catalytic testing for the epoxidation was conducted at different reactor temperatures, ranging from 150 °C to 300 °C. Two different gas feeds were used for the testing, with the following gas compositions: 88 v.% He, 6 v.% O<sub>2</sub>, 6 v.% C<sub>2</sub>H<sub>4</sub> for “Feed A”; 92 v.% He, 6 v.% O<sub>2</sub>, 2 v.% C<sub>2</sub>H<sub>4</sub> for “Feed B”. Both feeds were used with a gas flow of 50 NmL/min.

For the fixed bed reactor in this experimental setup: **WSHV = 10 mL/h·mg**.

From the data obtained in the catalytic testing, ethylene conversion, oxygen conversion and ethylene oxide selectivity were calculated using the following formulas:

$$\text{Equation 9: } C_2H_4 \text{ Conversion (\%)} = \frac{[CO_2]_{out}/2 + [EO]_{out} + [AA]_{out}}{[C_2H_4]_{out} + [CO_2]_{out}/2 + [EO]_{out} + [AA]_{out}} \cdot 100$$

$$\text{Equation 10: } O_2 \text{ Conversion (\%)} = \frac{[CO_2]_{out} + [EO]_{out}/2 + [AA]_{out}/2}{[O_2]_{out} + [CO_2]_{out} + [EO]_{out}/2 + [AA]_{out}/2} \cdot 100$$

$$\text{Equation 11: } EO \text{ Selectivity (\%)} = \frac{[EO]_{out}}{[CO_2]_{out}/2 + [EO]_{out} + [AA]_{out}} \cdot 100$$

#### ***4.4.- Characterization techniques***

This section details the characterization techniques employed for analyzing the materials and samples obtained during the experimental work, specifying the scientific equipment used and the procedures carried out, if any.

##### **4.4.1.- Zeta potential**

This technique is used for measuring the electrostatic charges of particles in solution. Zeta potential analyses were performed for the titanosilicates, cordierite and CoPt<sub>3</sub> nanoparticles. The equipment used for the analysis was a *90Plus Particle Size Analyzer* from *Brookhaven Instruments Corporation (BIC)* with a SR-574 cell.

##### Sample preparation:

Small amounts of sample (a spatula tip) were suspended in KCl 1mM aqueous solutions and the suspensions adjusted to different pHs (*Cyberscan pH 2100, Eutech Instruments*;

*Hamilton Filltrode* probe with *Skylyte-CL* electrolyte) via  $\text{HNO}_3$  0.1M (*Panreac*),  $\text{KOH}$  0.1M (*Panreac*) and higher dilutions of these two solutions. Zeta potentials for the samples were measured at pH 2.5, 5, 8.5 and 11. For Z potential in ethanolic solution, the samples were suspended in EtOH (absolute, *Panreac*) and measured. Measurements were in all cases performed after a brief sonication.

#### **4.4.2.- Scanning Electron Microscopy (SEM) and Energy-dispersive X-ray Spectroscopy (EDX)**

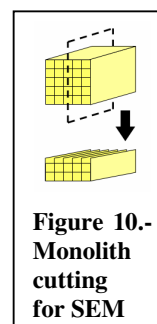
SEM was used for morphological analysis of the micrometric titanosilicate crystals and the titanosilicate layers grown on monoliths. This allowed assessment on whether or not the hydrothermal syntheses had proceeded correctly, as well as comparing some crystals phases of known morphology with images from the corresponding bibliography, although the identification had to be confirmed by XRD analysis.

An *INSPECT-F50* scanning electron microscope from *FEI* was used for these duties. The SEM microscope was equipped with a high resolution Schottky field emission gun. A variety of detectors, of which the secondary electron detector (SED), back-scattered electron detector (BSED), and an energy-dispersive X-ray detector (EDS) are the ones of interest to us, could be used in the microscope. The vacuum system comprised a conventional pump and a turbomolecular pump for high vacuum.

##### Sample preparation:

Powder samples were extended over carbon tape on the sample holder.

Monoliths were cut into two pieces through one of their channels, parallel to its longitudinal axis, using a utility knife (*Figure 10*). One of the two monolith fragments was then fixed to the sample holder using copper tape and carbon paste.



Particle size characterizations of the samples analyzed by SEM were performed by processing the microscope images with the *IMAQ Vision Builder* software.

Additionally, using the SEM microscope's EDS detector, energy-dispersive X-ray spectroscopy can be performed on the samples for assessing the weight and atomic compositions of the titanosilicate crystals and layers as well as the presence and distribution of the corresponding active metals deposited onto the layers.

#### **4.4.3.- Transmission Electron Microscopy (TEM)**

The TEM microscope was used to characterize the morphology, particle size and distribution of the deposited active metals on the titanosilicate supports.

The microscope used was a *Tecnai T20 (FEI)*, equipped with a Field Emission gun, capable of an acceleration voltage of 200 kV and able to image samples on TEM and STEM modes.

##### Sample preparation:

A small amount (a spatula tip) of the powder sample is suspended in ethanol and sonicated in an ultrasonic bath for a few minutes. A drop of the suspension is then deposited onto a TEM grid (Formvar Carbon Film on 200mesh Copper, *Electron Microscopy Sciences*) and left to dry at room temperature.

Particle size characterizations of the samples analyzed by TEM were performed by processing the microscope images with the *IMAQ Vision Builder* software.

#### **4.4.4.- X-ray Diffraction (XRD)**

The titanosilicate powders and CoPt<sub>3</sub> NPs were analyzed by X-ray diffraction to identify the crystallographic phases present in the samples.

The XRD measurements were performed in the “*Servicio de Difracción de Rayos X y Análisis por Fluorescencia*”, “*Servicio General de Apoyo a la Investigación*” of the University of Zaragoza. Data were collected at room temperature with a *RIGAKU “D-Max/2500”* diffractometer working at 40 kV and 80 mA, with a rotatory Cu anode and a graphite monochromator for selecting Cu K<sub>α</sub> radiation. XRD spectra were collected from  $2\theta = 5^\circ$  to  $45^\circ$  (for the titanosilicate samples) or from  $2\theta = 20^\circ$  to  $90^\circ$  (for the CoPt<sub>3</sub> nanoparticles), with  $0.03^\circ$  steps and measurement times of 1s/step.

Experimental results from the samples were compared with XRD simulations of the pure phases which had been obtained from the *Crystallography Open Database* webpage and processed with *Mercury* software.

#### **4.4.5.- Microwave Plasma Atomic Emission Spectroscopy (MP-AES)**

Atomic Emission Spectroscopy was performed after digestion of the powder samples to determine the true loading of the catalyst metals on each sample. The analyses were performed in a *4100 MP-AES (Agilent Technologies)* which creates an Ar plasma induced by microwaves.

#### Sample preparation (samples containing Ag):

9 mg of catalytic powder were added to 10 mL of a H<sub>2</sub>SO<sub>4</sub>/H<sub>3</sub>PO<sub>4</sub> 1:1 acid mixture in a teflon autoclave and dissolved by heating in a microwave oven (*ETHOS PLUS High Performance Microwave Labstation, MILESTONE Microwave Laboratory Systems*) at 20 °C/min until 200 °C were reached, temperature which was maintained for 20 min. When the autoclave was at room temperature, its contents were transferred to a 25 mL volumetric flask and brought to that volume with deionized water. From this solution, 2 mL were transferred to a 10 mL volumetric flask and diluted to that volume with water. Based on the expected silver content, a 5-point calibration curve was prepared in 50 mL flasks. To avoid differences in the signal background between sample and standards, a 20% (10 mL) of H<sub>2</sub>SO<sub>4</sub>/H<sub>3</sub>PO<sub>4</sub> 1:1 acid mixture was added to each calibration standard.

#### Sample preparation (samples containing Pt or Pt/Co):

20 mg of powder were added to 20 mL of aqua regia. The microwave heating procedure was identical to the one used for the silver samples. The autoclave contents were transferred to a 25 mL volumetric flask and brought to that volume with deionized water. From the this solution, 4 mL were taken and diluted in a 10 mL volumetric flask with deionized water. Based on the expected contents of the samples, a 5-point calibration curve was prepared for both metals in 50 mL flasks. To avoid differences in the signal background between sample and standards, a 40% (20 mL) of aqua regia was added to each calibration standard.

#### **4.4.6.- Thermogravimetric Analysis (TGA)**

Thermogravimetric analysis of the metal precursors (AgNO<sub>3</sub>, [Pt(NH<sub>3</sub>)<sub>4</sub>](NO<sub>3</sub>)<sub>2</sub>) and of PEI were performed in order to establish the minimum temperature required for their decomposition. Analyses were performed in a *METTLER-TOLEDO TGA/SDTA 851<sup>e</sup>*. No sample preparation was required. Approximately 5 mg of the sample (real weight must be known with precision) are introduced in a teflon crucible inside the equipment's furnace, which is heated from 40 to 600 °C at a rate of 10 °C/min.

(These TGA analyses are shown in *Figure A 1* in the Appendix).

## 5.- Results and discussion

### 5.1.- Catalytic powders

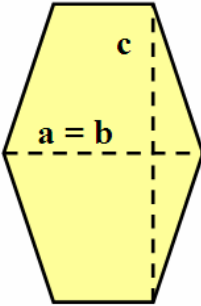
#### 5.1.1.- Titanosilicate supports characterization

This section will cover the results observed and the data obtained from the characterization of the synthesized titanosilicate crystals.

##### ETS-10

Several ETS-10 batches were synthesized during the course of the project which had slightly different characteristics. *Table 4* collects specific data from these syntheses.

**Table 4.- Summary of information from the synthesized ETS-10 crystal batches. Crystal sizes were only measured for selected batches.**

<i>Batch code</i>	<i>Gel pH</i>	<i>Yield</i>	<i>Crystal size (<math>\mu\text{m}</math>)</i>	<i>Crystal morphology</i>
ETS-10 B1	10,1	63,81%	a = $0.55 \pm 0.14$ c = $0.81 \pm 0.17$	
ETS-10 B2	10,1	60,17%	-	
ETS-10 B3	10,4	57,09%	-	
ETS-10 B4	10,4	45,64%	-	
ETS-10 B5	10,4	72,89%	a = $0.26 \pm 0.08$ c = $0.41 \pm 0.09$	
ETS-10 B7	10,4	65,68%	a = $0.35 \pm 0.05$ c = $0.43 \pm 0.11$	

As can be seen in the table, the yield of the hydrothermal synthesis (method “ETS-10 TiO<sub>2</sub>”) was found to vary between 45% and 75% (yield based on Ti, the limiting agent). The variability doesn’t seem to arise from the pH adjustment of the gel, which would be the obvious choice, so we cannot assure which parameter is responsible for this.

The powder diffraction patterns from the selected batches B1, B5 and B7 are shown in *Figure 11*. The patterns are compared with a simulation diffractogram of ETS-10<sup>[26]</sup>. For the three samples, all the peaks corresponding to the simulation can be found, thus confirming the presence of ETS-10 in the batches. The sample patterns show two wide peaks at 5.90° and 29.85° (not marked in the figure) that belong to ETS-10 despite not correlating with the ETS-10 simulation spectrum. These two peaks appear in every experimental XRD analysis we have performed on our ETS-10 samples (including TiCl<sub>3</sub> route syntheses, which rules out anatase as the source of those peaks), and even in



bibliography, disregarding purity of samples<sup>[5,20]</sup>. Additionally, another two peaks can be found in all the diffractograms (marked with x in the figure). These peaks belong to quartz impurities, which was expected, since quartz has been reported previously as the main impurity appearing in TiO<sub>2</sub>-based ETS-10 syntheses<sup>[5]</sup>. It is here where the pH value plays an important role, since it has a great effect on the amount of impurities present in the obtained powder. In *Figure 11* it can be observed that the intensity of the quartz peaks for B1, which was adjusted to pH 10.1, is much higher than for B5 or B7, both of them adjusted to pH 10.4. The intensity of the ETS-10 peaks for these two batches is also higher than in the B1 pattern. These experimental results indicate that batches synthesized after adjusting the pH value to 10.4 are of higher purity. This is in accordance with what was reported by Rocha et al.<sup>[19]</sup>, who recommended pH around 10.4 for obtaining high purity ETS-10 crystals. An unidentified peak remains in the B1 pattern, but other impurities from the anatase synthesis were neither expected nor found, since the crystallization of ETS-4 happens at higher pH<sup>[5]</sup>.

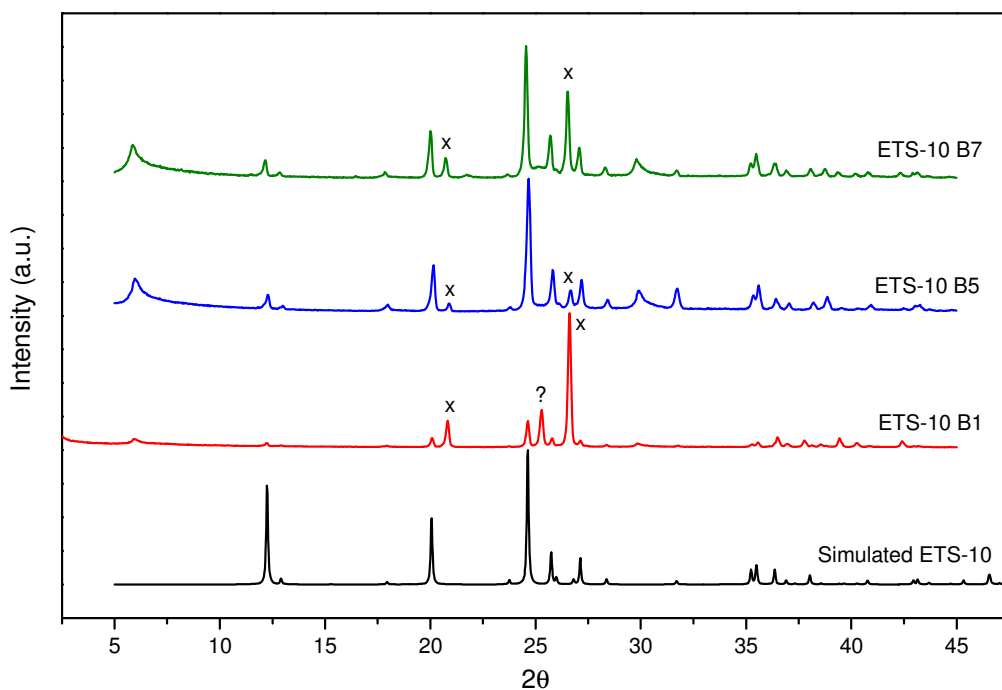
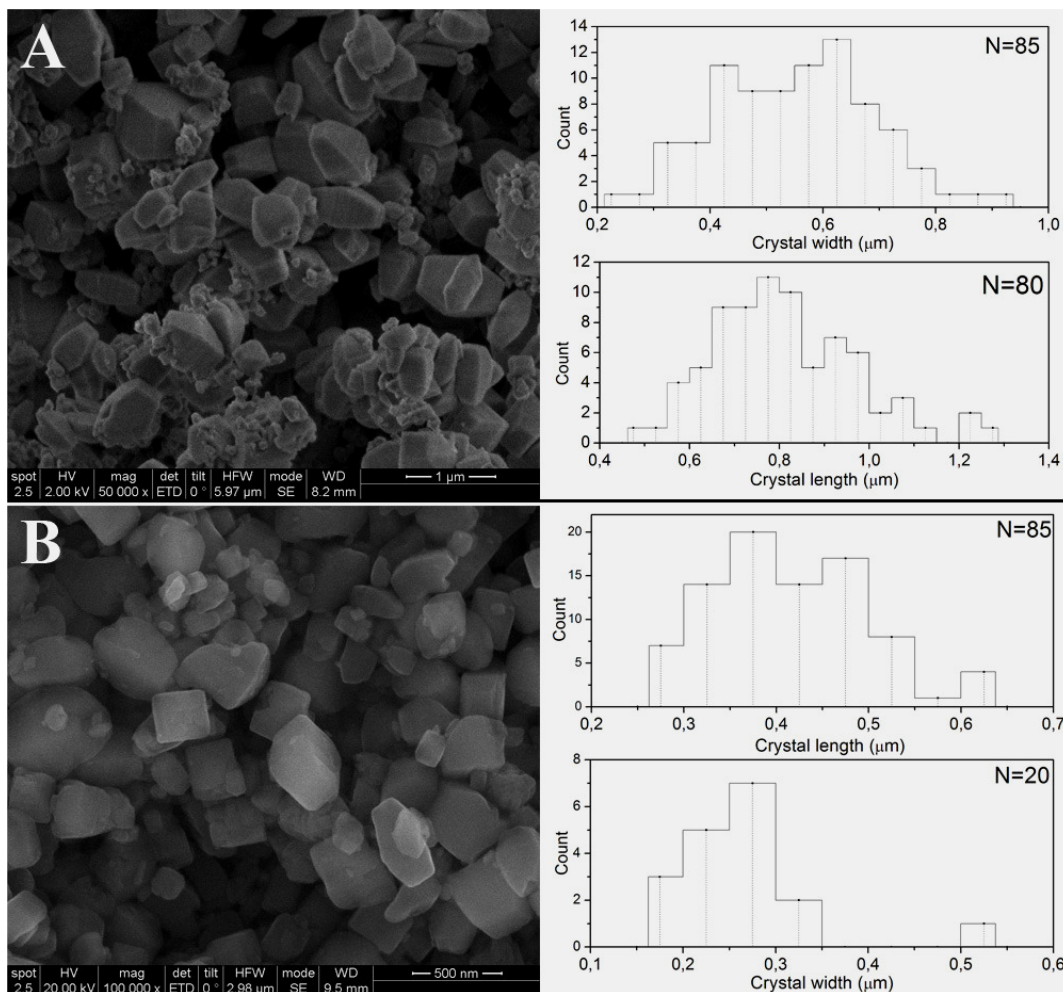


**Figure 11.- XRD spectra from simulated ETS-10<sup>[26]</sup> and from experimental batches B1, B5 and B7. Peaks marked with x correspond to quartz impurities<sup>[27]</sup>.**

The crystals of these batches were also analyzed by SEM (*Figure 12* shows crystals of B1 and B5 with their corresponding histograms; Additional images for B1, B5 and B7 can be seen in the Appendix, *Figure A 2* to *Figure A 4*). The images show that the crystals have a truncated bipyramid morphology, thus being in accordance with the

reported morphology of ETS-10 synthesized by the Anatase route<sup>[20]</sup>. The purity of each batch, already discussed before, is in correlation with the amount of amorphous material or impurities which can be seen in the images. B1, with pH 10.1 and a higher amount of quartz impurities (according to *Figure 11*) presents a “dirtier” look than B5 and B7, with pH 10.4 and higher sample purity.

Average crystal sizes (shown before in *Table 4*) of the synthesized batches with pH 10.4 are in agreement with reported values of  $\sim 0.3 \mu\text{m} \times \sim 0.4 \mu\text{m}$  ( $a=b \times c$ )<sup>[20]</sup>. Batches adjusted to pH 10.1 maintained the same shape and crystal habit (as has been indicated) but showed a larger crystal size ( $0.55 \times 0.81 \mu\text{m}$ ).

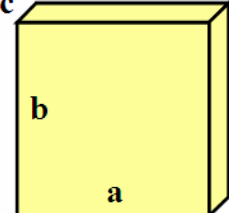


**Figure 12.- SEM images of ETS-10 crystals from batches B1 (A) and B5 (B), accompanied by the histograms obtained from the particle size distribution analysis.**

### Synthesis of JDF-L1

The titanosilicate JDF-L1 was synthesized both by unseeded and by seeded hydrothermal syntheses. *Table 5* collects information on the synthesized batches.

**Table 5.- Summary of information from the synthesized JDF-L1 crystal batches.**

<i>Batch code</i>	<i>Yield</i>	<i>Crystal size (<math>\mu\text{m}</math>)</i>	<i>Crystal morphology</i>
JDF-L1 B1	93,78%	-	
		-	
JDF-L1 B2	94,58%	$a = 52.87 \pm 6.31$	
		$c = 0.65 \pm 0.14$	
JDF-L1 B2-S	98,62%	$a = 13.69 \pm 4.27$	
		$c = 0.50 \pm 0.12$	
JDF-L1 B3-S	97,65%	$a = 5.90 \pm 1.48$	
		$c = 0.21 \pm 0.06$	

Two batches (JDF-L1 B1 and B2) were synthesized following the unseeded synthesis procedure (*JDF-L1 TiCl<sub>3</sub> method*). Another three batches of the layered titanosilicate (JDF-L1 B1-S, B2-S and B3-S) were synthesized by the seeded synthesis procedure (*JDF-L1 TiCl<sub>3</sub>-S method*). For B1-S and B2-S, the powders obtained from B1 and B2, respectively, were grounded and used as seeds; for B3-S, seeds were provided by César Rubio from the CREG group of the Institute of Nanoscience of Aragón. The yield of both synthesis methods was very high, more so for the seeded synthesis.

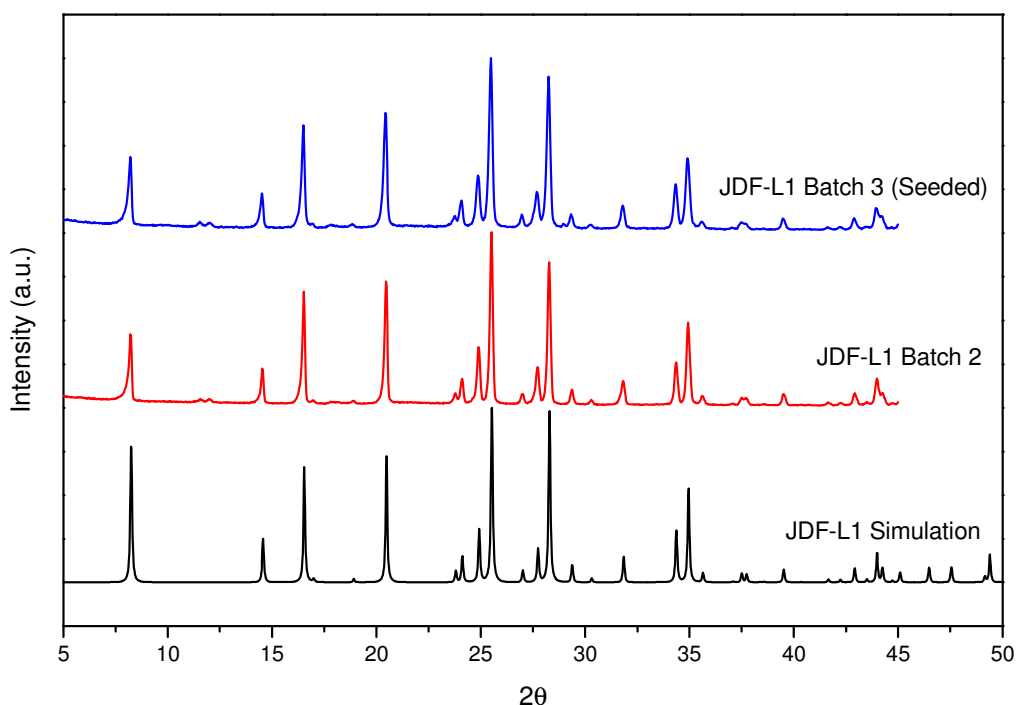


**Figure 13.- XRD spectra from simulated JDF-L1<sup>[28]</sup> and from experimental batches B2 and B3-S. No impurities identified.**

The powder diffraction patterns from the selected batches B2 and B3-S are shown in *Figure 13*. The patterns are compared with a simulation diffractogram of JDF-L1<sup>[28]</sup>.

This XRD analysis showed that the JDF-L1 crystals obtained in each synthesis were of high purity, since no other crystallographic phases but JDF-L1 can be identified with the spectra of B2 and B3-S. Additionally, not only peak position but also the intensity of each peak fits very well with the simulation of the material used for the identification.

SEM images of the batches reveal that the crystals obtained by the unseeded synthesis are somewhat large (~50  $\mu\text{m}$ ) which renders them inappropriate for the monolith seeding procedures. However, smaller crystals of JDF-L1 (5-10  $\mu\text{m}$ ) were obtained by the seeded hydrothermal synthesis. The observed morphology of the crystals, square or rectangular sheets, is the expected for the laminated titanosilicate. The sheets from the unseeded syntheses (B2, *Figure 14*) are, however, densely grouped up in big bundles. The crystal sheets from the seeded syntheses (B2-S, *Figure 14*) are grouped in smaller bundles, mainly due to the smaller sheet size, but also the bundles are more “open” or “loose”, as seen in *Figure 15* for B3-S.

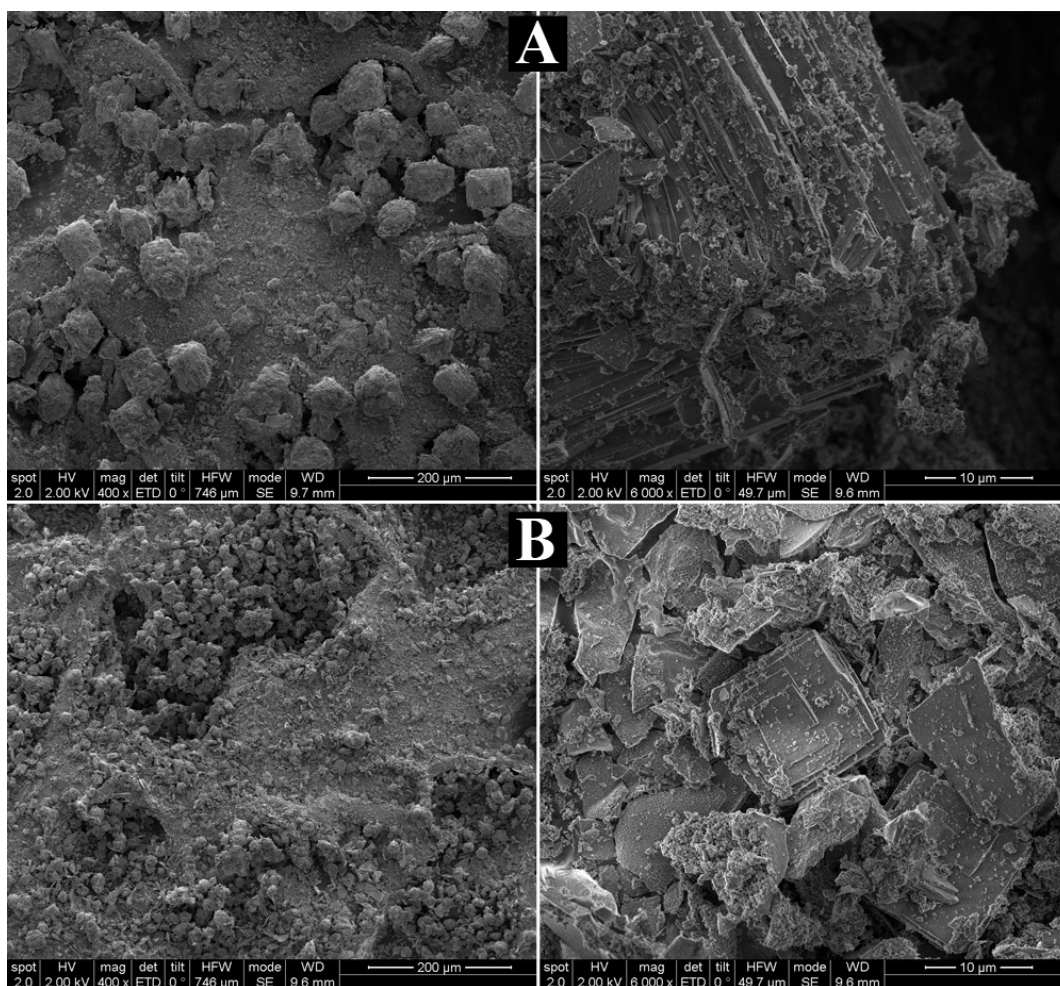
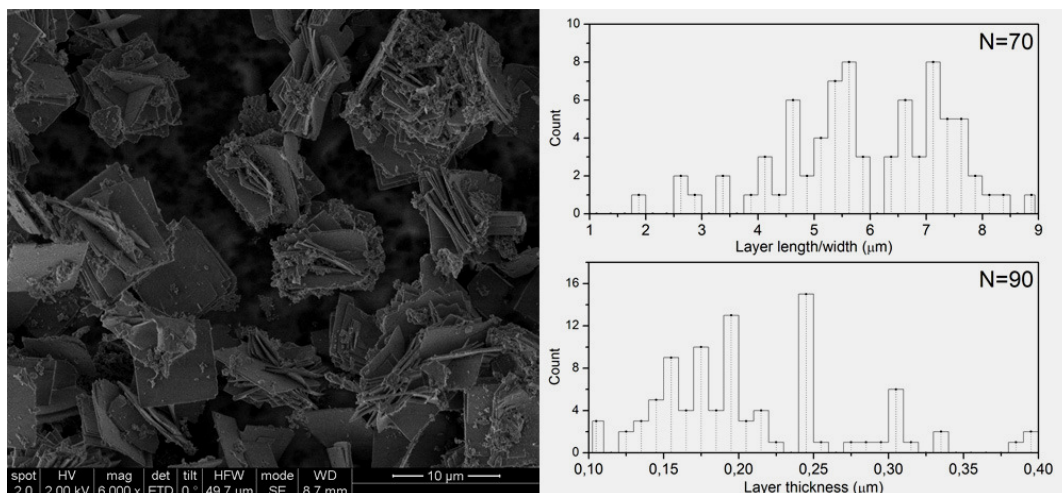


Figure 14.- SEM images of JDF-L1 crystals. A) JDF-L1 B2; B) JDF-L1 B2-S.



**Figure 15.- SEM image of JDF-L1 B3-S and its size distribution histogram.**

The size distribution analysis performed for B2 and B3-S provided average sizes in agreement with the expected crystal size of the unseeded and seeded syntheses, according to bibliography<sup>[21]</sup>. However, B2-S crystals were bigger in size than those from B3-S synthesis. The explanation we suggest to justify this size difference is that the initial size of the seeds has a great influence on the final crystal size. For B2-S, B2 crystals were grounded as seeds, and they probably were quite large even after the grounding. For B3-S, we used 3 μm seeds provided by the CREG group, and it is reasonable that their small size meant more seeds in the same amount of powder, so a high number of crystals translates into an overall small growth.

Additional images of B3-S crystals are available in the Appendix, *Figure A 5*.

### **5.1.2.- CoPt<sub>3</sub> nanoparticles characterization**

The metallic particles were analyzed by XRD and the powder diffraction pattern is shown in *Figure 16*. The peaks in the diffractogram are very broad due to the small size of these metallic particles. It can be seen in the diffractogram that the peaks correlate reasonably to the CoPt<sub>3</sub> metallic phase. However, peaks expected for pure Pt are also reasonably close to the particle diffraction peaks, but the possibility of having Pt and Co metallic phases and not the bimetallic compound can be discarded given that none of the peaks could be correlated with the metallic Co phase. There is another bimetallic phase, CoPt, that could have been formed in the synthesis, but this possibility is also discarded as none of its peaks are present in the sample's diffractogram. However, the diffraction patterns present a series of very intense, narrow peaks that do not belong to any of these metals and their combined phases. These peaks have been identified as NaCl, which

could be formed in the synthesis since there are sodium and chlorine ions in solution (from NaBH<sub>4</sub> and from the metal precursors, respectively).

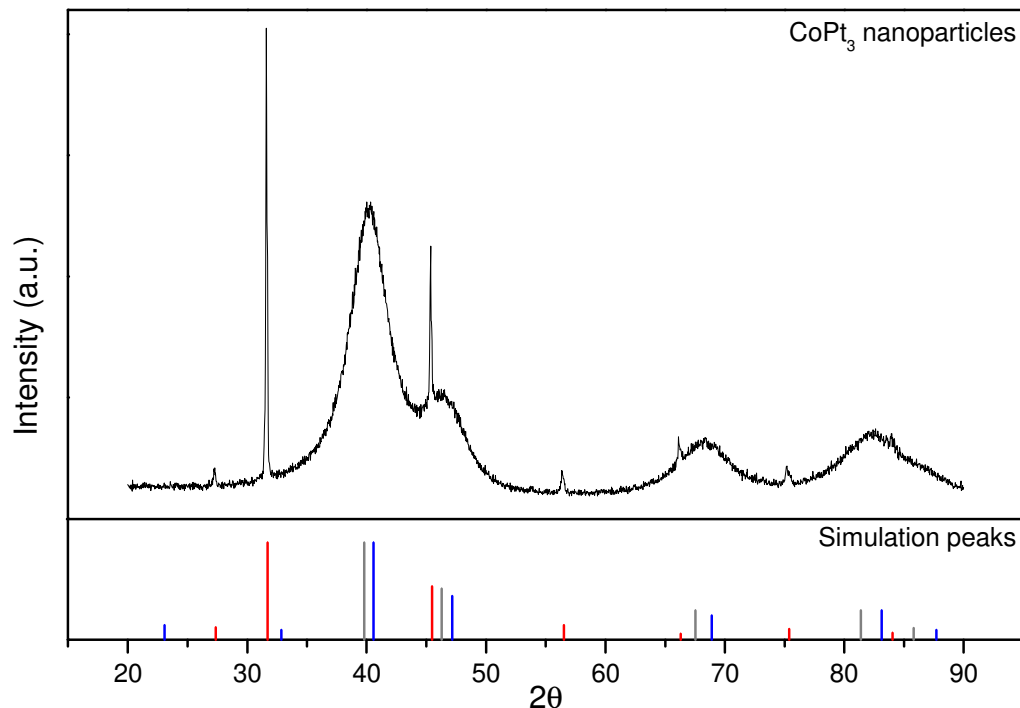


**Figure 16.- XRD spectra of the CoPt<sub>3</sub> NPs and reference peak locations (from ICDD) for NaCl (red), Pt (grey) and CoPt<sub>3</sub> (blue).**

The *Scherrer equation* (Equation 12), was used to estimate the particle size. Taking  $K = 0.94$  and  $\lambda_{\text{Cu K}\alpha} = 0.154 \text{ nm}$ , and using the peak at  $2\theta = 40.18^\circ$  which has a broadening of  $4.06^\circ$  or  $0.0709 \text{ rads}$ , the *particle size (L) is estimated as 2.17 nm*.

$$\text{Equation 12: } B = \frac{K\lambda}{L \cos \theta}$$

The CoPt<sub>3</sub> nanoparticles were also studied in TEM to assess the morphology and particle size. A selected picture and the histogram obtained from the size distribution analysis are shown in *Figure 17*. Despite having kept the particles in ethanol without any drying process after the synthesis, and the vigorous sonication they were subjected to before preparing the TEM grid, images show that the nanoparticles are agglomerated. According to the size distribution analysis from the TEM images, the **average particle size** was **3.34 ± 0.58 nm**, slightly larger than the estimation from the XRD data, but in agreement the results obtained by other authors using the same method<sup>[22]</sup>.

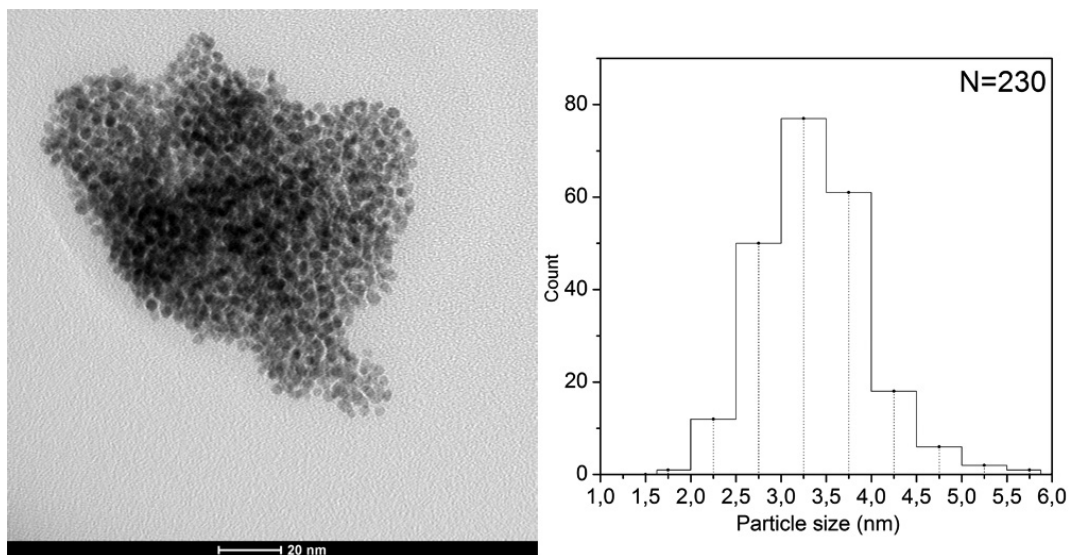


Figure 17.- TEM image of CoPt<sub>3</sub> nanoparticles and the particle size distribution histogram.

Since the deposition techniques involve electrostatic interactions, the zeta potential of the titanosilicates, cordierite and bimetallic nanoparticles were measured in water at different pH and in ethanol (see *Figure 18*). The titanosilicates and the bimetallic nanoparticles present negative surface charges in water or ethanol solutions. In the case of cordierite the surface is positively charged at pH=2. The interactions between any two of these samples will be repulsive (except cordierite at low pH). For this reason the surfaces of titanosilicates and cordierite were positively charge using a cationic polymer, see section 4.2.2.-.

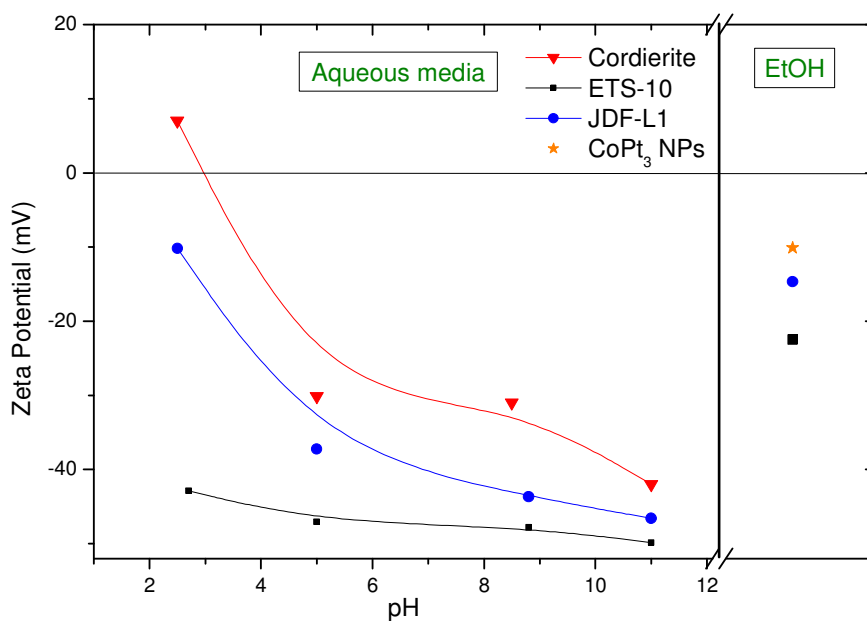


Figure 18.- Zeta potential vs pH representation of the samples. Values of zeta potential in ethanolic solution are shown in the right section of the graph. Tabulated values available in *Table A 1*.

### 5.1.3.- Catalytic powder characterization

Once the catalytic supports were synthesized and ready, the active metal phases were deposited by different means and a variety of catalytic powders were prepared. *Table 6* collects some fundamental information about these powders.

**Table 6.- Summary of prepared catalytic powders and their characteristics. \*=Value obtained for the individual NPs in *Figure 17*.**

<i>Catalytic powder</i>	<i>Deposition method</i>	<i>Theoretical loading (wt.%)</i>	<i>Experimental loading (wt.%)</i>	<i>Metal particle size (nm)</i>
<b>Ag-ETS-10</b>	<i>Impregnation</i>	15%	12.72 ± 0.10	4.59 ± 2.43
	<i>Ion Exchange</i>	<15%	5.86 ± 0.38	10.08 ± 3.96
<b>Ag-JDF-L1</b>	<i>Impregnation</i>	15%	13.62 ± 0.26	7.52 ± 4.40
<b>Pt-JDF-L1</b>	<i>Ion Exchange</i>	<1.7%	1.14 ± 0.04	2.64 ± 0.65
<b>CoPt<sub>3</sub>-JDF-L1</b>	<i>Electrostatic stabilization</i>	3% NPs (0.27% Co; 2.73% Pt)	2.15 ± 0.26 NPs (0.18% Co; 1.97% Pt) Atomic Pt/Co ratio = 3.24	3.34 ± 0.58 *

The catalytic powders' metal contents were studied by atomic emission spectroscopy, and the experimental loadings determined in the analysis are shown in *Table 6*. Silver loadings for the impregnated samples were very similar to the theoretical values, as expected from this deposition method, though some of the metal mass has been lost in some of the treatment steps. For the ion-exchanged samples, due to the equilibrium process involved, loadings are much lower than the theoretical value. Platinum is more easily exchanged than silver, and this could be attributed to the smaller size of the ionic radius of Pt<sup>2+</sup>, 0.7 Å vs 1.26 Å in the case of Ag<sup>+</sup>. The procedure for depositing CoPt<sub>3</sub> is similar to an impregnation method (see section 4.1.3.-). As a result the loading is near to the theoretical value. The difference could be attributed to an error in the calculation of the mass concentration of the solution of the NPs, since the PVP stabilizing the NPs has not been considered. The weight percentages of Co and Pt, once transformed into moles, provide an **atomic Pt/Co ratio of 3.24**, very close to the theoretical value of **3** expected if the metal phase is CoPt<sub>3</sub>.

Particle sizes of the deposited metals were averaged from size distribution analyses of TEM images of the supported catalysts. These images and the histograms obtained from them are included in the Appendix, *Figure A 6* and *Figure A 7*.



It is important to note that during calcination after depositing or exchanging the metal ions, the annealing process not only reduces the ions into metallic phase, but since it is a high temperature treatment, it also causes a migration of part of the guest metal atoms out of the internal cavities of the titanosilicate, leading to the formation of big particles of the metal on the surface of the titanosilicate crystals, as reported in various studies for the case of silver in ETS-10<sup>[29]</sup>. As a general rule (see section 3.1.-) for heterogeneous metal catalysts it is preferred that the active metal particles have the smallest size possible, for an enhanced surface/volume ratio which favours catalytic activity. In the case of the Pt-based catalyst, the particle size is 2.6 nm, small enough to achieve high catalytic activity, and no big particles were observed. However, the particle size increase is not necessarily a problem for our Ag-based catalytic powders due to the characteristics reported for silver in ethylene epoxidation<sup>[30,31]</sup>.

## 5.2.- Structured catalytic microreactors

### 5.2.1.- Seeding of cordierite monoliths

Different approaches were selected for seeding the monoliths with small titanosilicate crystals (listed in *Table 2*). The amount of seeding achieved by the different methodologies conducted is expressed as relative weight gains  $[100 \cdot (M_0 - M_{seeds}) / M_0]$  and the average results are collected in *Table 7*. The weight gain values of all the monoliths prepared are detailed in the Appendix (*Table A 2*).

**Table 7.- Average weight gain of monoliths after ETS-10 seed deposition by different methods.**

<i>Seeding Method</i>	<i>Average Gain<sub>seed</sub> (%)</i>
<b>Sonication (13 wt.%)</b>	<b>8.26 ± 2.33</b>
<b>Sonication (2.5 wt.%)</b>	<b>3.34 ± 1.72</b>
<b>LbL by ES (PEI)</b>	<b>1.05 ± 0.23</b>
<b>LbL by ES (PDDA)</b>	<b>0.22 ± 0.21</b>
<b>Dip Coating</b>	<b>7.18 ± 1.83</b>

Apart from the method itself, there are a variety of different factors that have an effect on the final loading and the coating quality, such as the properties of the slurry (given by the properties of the solids, the solvent, and the amount of solid). It is known that by varying the powder concentration in the slurry and the number of immersions, loading and film thickness can be adjusted. These parameters are also affected by the rate of blowing air used in the drying steps<sup>[23]</sup>. A comparison between the two *sonications*,

differing only in the amount of solid in the seed suspension, brings forward the truthfulness of the previous statements. Whereas the method with a 13% of ETS-10 seeds in suspension yielded, overall, well and homogeneously coated monoliths (as seen by SEM, *Figure 19*) with an average seed loading of 8%, the one with 2.5% of seeds in suspension proved to be less effective, and the seeded monoliths, with an average seed loading of 3%, showed incomplete coverage of the monolith wall surface. As a *home-made rule of thumb developed during the experimentation with these procedures, the threshold between good or insufficient coverage of the monolith can be set at a 6 wt.% of loading*. Those monoliths below 6% loading usually presented deficient coatings, and above 6% presented homogeneously coated walls. **Dip coating** proved itself to be a reliable deposition method as well, with around 7% loadings and homogeneous coverage (see *Figure 19*). It has been reported that for zeolite-type materials, obtaining high loadings on monoliths can be difficult to achieve, even after hydrothermal syntheses. Usual loadings are in the 5-20 wt.% range<sup>[32]</sup>, so these results are satisfactory.

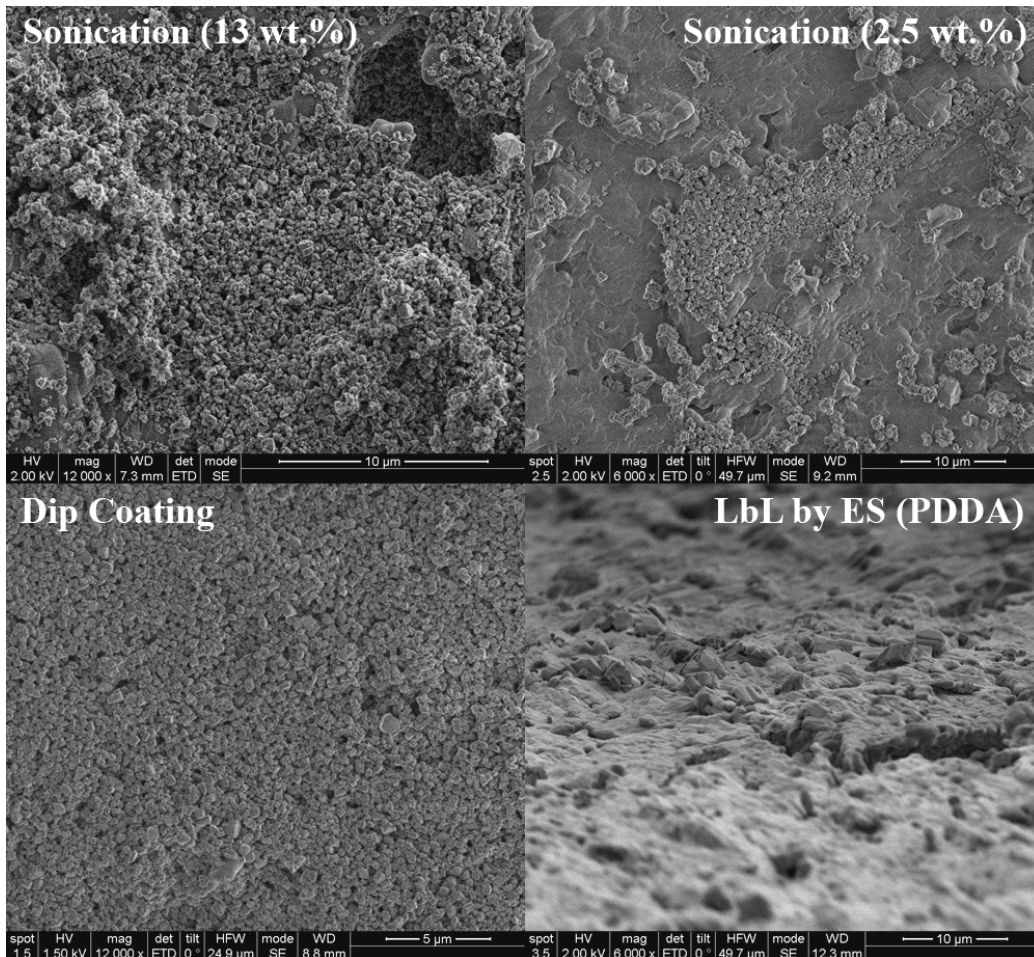


**Figure 19.- SEM images of ETS-10 coatings on monoliths deposited by different methods.**

It has been stated before, and shown in *Figure 18*, that cordierite and the titanosilicate seeds have same sign superficial charges, which means there should be repulsive behaviour between these materials, and the reason why layer by layer deposition by electrostatic stabilization was tested. However, the good loading results shown before could be explained by the adhesion of the coating or seed layer taking place primarily by a mechanical mechanism in which the particles anchor and interlock themselves on the surface irregularities of the support<sup>[11]</sup>. Being particles of a relatively big size, superficial charge interactions seem to be negligible, given the results obtained.

Regarding the ***Layer by layer deposition procedures***, a good coverage of the support should be obtained according to certain sources<sup>[23,24]</sup>. However, the loadings were very unsatisfactory for both of the tested cationic polymers. This may be explained by the polymer hindering the anchoring and interlocking of the crystals with the monolith defects and rugosities, and the low amount of seeds in the suspension.

The sonication method with suspensions of 13 wt.% and 6 wt.% of seeds was selected for deposition of JDF-L1 crystal sheets. The former suspension sedimented very fast and caused blocking of the monolith channels, rendering the monolith unusable. The latter suspension allowed deposition without blocking, but the loadings were inferior to 2%. Other deposition methods were directly discarded. The difficulty of seeding the monoliths with this titanosilicate probably arises from the size of the seeds. While ETS-10 crystals had sizes around 0.4  $\mu\text{m}$ , the JDF-L1 sheets were of 3-5  $\mu\text{m}$ , if not bigger, which hinders the movement of the crystals into the monolith channels, and the anchoring to the wall.

### **5.2.2.- Titanosilicate growth on cordierite monoliths**

Several synthesis gels and parameters (see *Table 3*) were tested for growing a titanosilicate layer inside the seeded monoliths. However, most of these methods did not provide the desired results (sufficient loading and wall coverage, homogeneous distribution of the crystal layer, etc) and they will not be disclosed here. From all the synthesis gels and methods tested, ***TiCl<sub>3</sub>-A*** was the most reliable and offered the most homogeneous results, both in terms of coverage and crystal phases present. The ***TiCl<sub>3</sub>-A/R*** procedure was identical, but the hydrothermal synthesis was performed in a rotatory oven. These methods were the most significative and their results will be discussed further. The relative growth and total weight gains for each monolith as well as the average values for each method, are collected in *Table 8* and *Table 9*.

**Table 8.- Relative weight gain of monoliths after growth by different hydrothermal synthesis methods. Seeding of the monoliths was performed by *Sonication* (13 wt.%).**

<i>Monolith</i>	<i>Crystal growth method</i>	<i>Gain<sub>growth</sub> (%)</i>	<i>Gain<sub>total</sub> (%)</i>
M15	<i>TiCl<sub>3</sub>-A</i>	11,67	21,13
M17		11,33	22,08
M24		13,02	23,59
M27		17,45	27,35
M28		13,13	22,11
M29		8,95	17,31
M30		9,40	19,14
M34		8,63	20,85
M37		15,24	28,30
M40		8,08	17,48
M41		9,32	19,85
M31	<i>TiCl<sub>3</sub>-A/R</i>	6,39	15,35
M32		6,44	13,62
M33		4,45	11,76
M35		6,72	16,99

**Table 9.- Average relative gains and average mass of the catalytic support achieved on monoliths after growth for each synthesis method.**

<i>Method</i>	<i>Average Gain<sub>growth</sub> (%)</i>	<i>Average Gain<sub>total</sub> (%)</i>	<i>Average total mass of titanosilicate support (mg)</i>
<i>TiCl<sub>3</sub>-A</i>	11.47 ± 3.00	21.74 ± 3.57	163.8 ± 22.1
<i>TiCl<sub>3</sub>-A/R</i>	6.00 ± 1.04	14.43 ± 2.25	104.1 ± 18.4

A chosen example of titanosilicate layer grown by the *TiCl<sub>3</sub>-A* method is shown in the SEM image of *Figure 20*, along with the size distribution histogram of the observed crystals. The thickness of the titanosilicate layer was measured from SEM images of a monolith cut transversally and embedded in resin, shown in *Figure 21*.

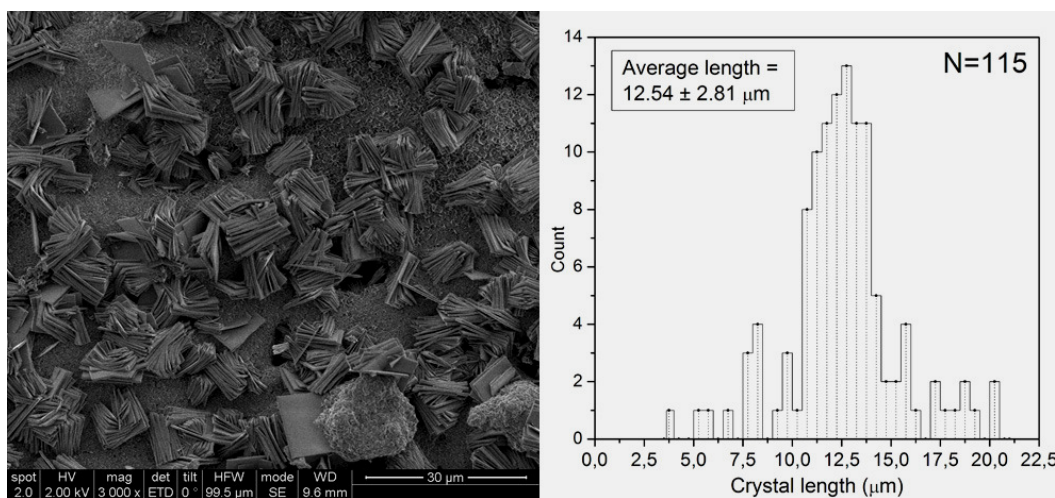


**Figure 20.- SEM image and size distribution histogram of crystals grown by the *TiCl<sub>3</sub>-A* method.**

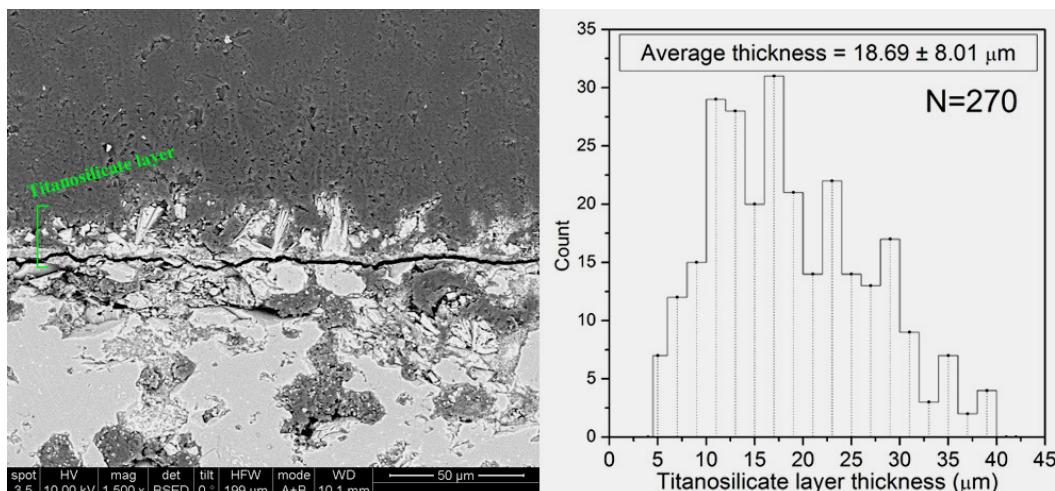


**Figure 21.-** Transversal SEM image of a monolith titanosilicate layer, with the corresponding size distribution histogram and the average thickness value.

In *Figure 20* it can be observed that the titanosilicate growth has not yielded a continuous or homogeneous layer. Instead, we have a homogeneous distribution of lots of laminated crystal bundles over a bed of an undefined phase which could be amorphous material. The observed crystals do not resemble ETS-10 usual morphology. In fact, the crystals are laminated, and look very similar to full grown JDF-L1. This crystal morphology is the majority, but small regions of the monolith present others (see *Figure A 9* in the Appendix for other morphologies observed on Monolith 24, used as characterization reference), though they suppose less than 5% of the coverage.

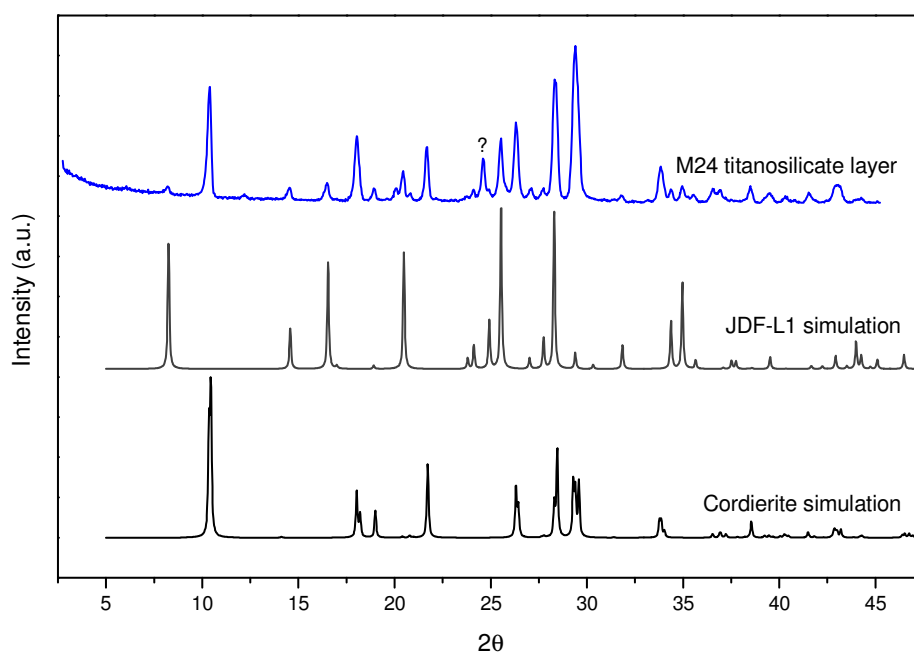


**Figure 22.-** XRD spectrum from Monolith 24's surface compared to JDF-L1<sup>[28]</sup> and Cordierite<sup>[33]</sup> simulation spectra.

An XRD analysis of the titanosilicates grown on Monolith 24's surface reveals that the main crystal phase observed is, indeed, JDF-L1 (see *Figure 22*). The rest of the peaks in the spectra correspond to cordierite. There is one unidentified peak at  $2\theta = 24.6^\circ$ . The other morphologies observed by SEM did not give any signal in the diffractogram.

The XRD analysis of the powder obtained from the leftover gel of the synthesis reveals the presence of both JDF-L1 and ETS-10 crystals (see *Figure 23*), with the usual crystal morphologies as observed by SEM imaging (see *Figure 24*).

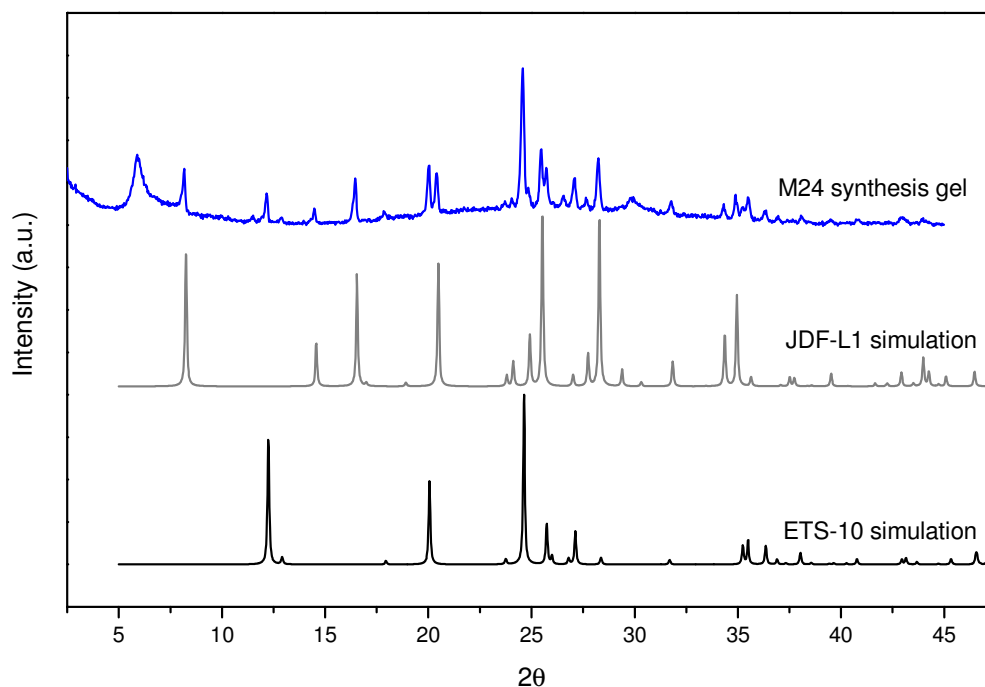


**Figure 23.-** XRD spectrum of the leftover gel from M24's synthesis, compared to JDF-L1<sup>[28]</sup> and ETS-10<sup>[26]</sup> simulation spectra.

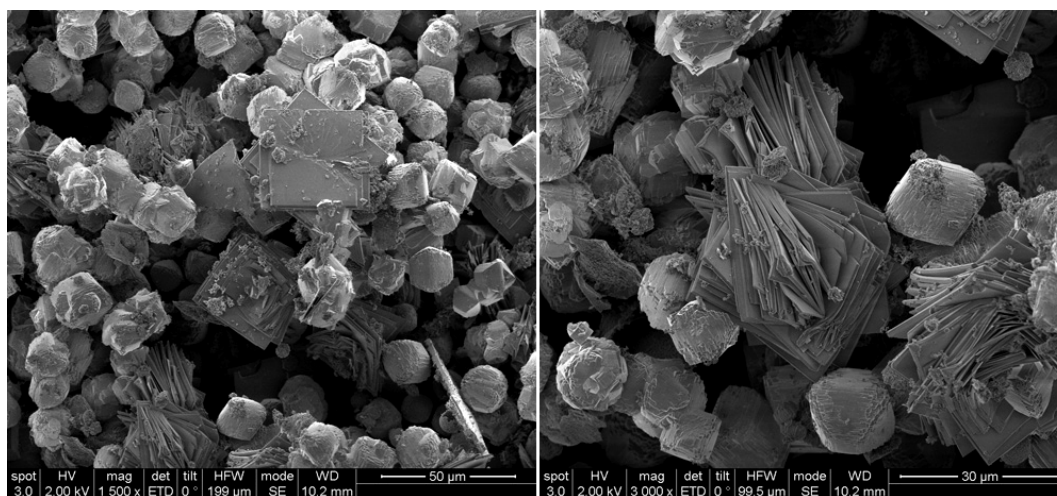


**Figure 24.-** SEM images of the leftover gel from M24's synthesis.

The observed change of crystal phase from seeds to grown crystal could be explained by one of the problems of the in situ synthesis of zeolites or titanosilicates on monolith supports, which is the lack that exists regarding the accessibility of molecules during the synthesis. This, along with the slow rate of renewal of the reagents in the solution or gel trapped inside the monolith channels could lead to another composition of the gel inside the channels, turning a gel initially designed for ETS-10 synthesis into a gel that more easily yields another crystal phase. This is the reason why the same hydrothermal synthesis was also conducted in rotatory ovens (*TiCl<sub>3</sub>-A/R*) to favour gel renewal inside the channels. The experiments performed in rotatory ovens, however, did not differ too much from static syntheses, obtaining the same crystal phase (JDF-L1) and similar homogeneity of coverage, but with lesser loadings of titanosilicate, as seen on *Table 9*.

### 5.2.3.- Active phase deposition in titanosilicate layers in monoliths

For preparing the final catalytic microreactors, monoliths with titanosilicate layers grown by the *TiCl<sub>3</sub>-A* method were used. These monoliths were subjected to the corresponding ion exchange procedures, for their use in either selective CO oxidation or ethylene epoxidation. The monoliths were cut in half and analyzed by SEM-EDX to assess their chemical compositions, but more specifically their metal contents, which are disclosed in *Table 10* and *Table 11*.

**Table 10.- Average chemical composition of an Ag-exchanged monolith by EDX analysis.**

<i>Element</i>	<b>O</b>	<b>Na</b>	<b>Mg</b>	<b>Al</b>	<b>Si</b>	<b>K</b>	<b>Ti</b>	<b>Ag</b>
<i>Weight %</i>	37.28	0.22	0.81	1.13	20.37	0.84	6.70	32.66
	±	±	±	±	±	±	±	±
	1.90	0.04	1.08	0.52	0.61	0.28	0.91	3.18
<i>Atomic %</i>	64.64	0.28	0.89	1.14	20.13	0.60	3.91	8.44
	±	±	±	±	±	±	±	±
	0.54	0.05	1.13	0.46	0.35	0.21	0.64	1.11

**Table 11.- Average chemical composition of a Pt-exchanged monolith by EDX analysis.**

<i>Element</i>	<b>O</b>	<b>Na</b>	<b>Mg</b>	<b>Al</b>	<b>Si</b>	<b>K</b>	<b>Ti</b>	<b>Pt</b>
<i>Weight %</i>	48.90	3.30	1.88	2.17	27.67	2.82	8.06	5.21
	±	±	±	±	±	±	±	±
	0.35	0.38	0.70	0.73	0.35	0.19	0.92	0.77
<i>Atomic %</i>	66.31	3.11	1.68	1.74	21.37	1.57	3.65	0.58
	±	±	±	±	±	±	±	±
	0.14	0.36	0.61	0.58	0.34	0.11	0.43	0.09

The Ag-exchanged monolith had ~190 mg of titanosilicate, so the maximum theoretical loading we could achieve was 31.6 wt.%, whereas for the Pt-exchanged monolith, with ~170 mg, the maximum loading would be 3 wt.%. As we see in the respective tables,

the experimental metal loadings, according to EDX, are higher than those theoretical values, so we can assume that the weight percentages for the active metals are being overestimated by the technique. The atomic percentages for the other studied elements are in fair correlation with the JDF-L1 unit formula. For example, Si/Ti ratios for the average EDX measurements are 5.15 for Ag-Monolith, and 5.86 for Pt-Monolith, whereas the JDF-L1 Si/Ti ratio is 4. The discrepancy can be attributed to Si of the cordierite below the titanosilicate layer being also measured, which can be assured due to the significant presence of Mg and Al (coming only from cordierite) in the analysis. However, specific EDX measurements of the crystals (not measuring the monolith background areas) gave Si/Ti ratios around 4.5, which is more reasonable.

The images taken during the EDX analysis (*Figure 25*) show big metal particles (~0.36  $\mu\text{m}$  Ag particles; ~0.16  $\mu\text{m}$  Pt particles). However, it is expected that the titanosilicate surfaces are covered by a majority of smaller sized particles, such as the ones in the powders, but SEM-EDX does not have enough resolution for confirming this.

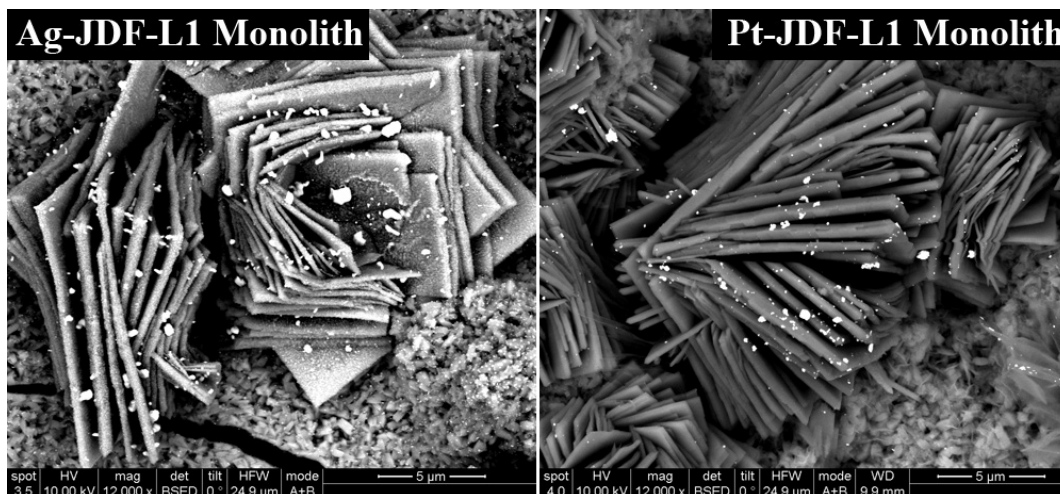


**Figure 25.- Metal particles observed on titanosilicate crystals of the ion-exchanged monoliths. Images obtained with a Backscattered electron detector.**

### ***5.3.-Catalytic activity testing***

#### **5.3.1.- Selective CO oxidation (SELOX)**

The reproducibility of the catalytic tests was assessed by repeating the measurements of certain experiments at each temperature while cooling the oven, not only when heating. *Figure 26* and *Figure 27* show the experiments for Pt-JDF-L1 powder and monolith microreactor.



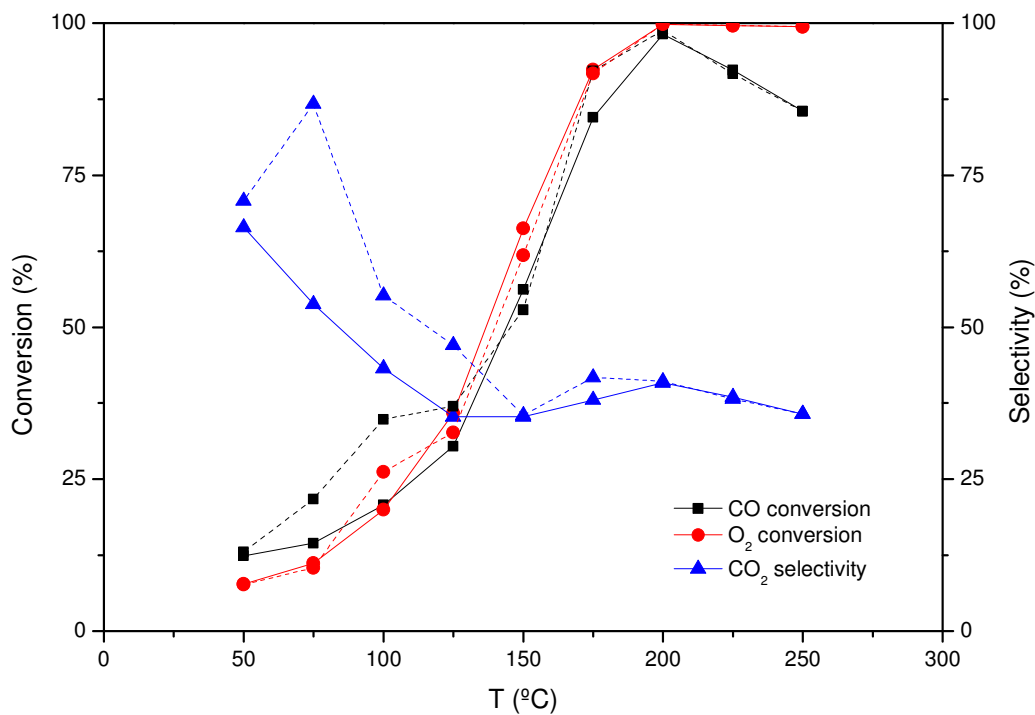


Figure 26.- Pt-JDF-L1 Powder (1.14% Pt). WHSV = 30 mL/h·mg. Solid lines: increasing temperature. Dashed lines: decreasing temperature.

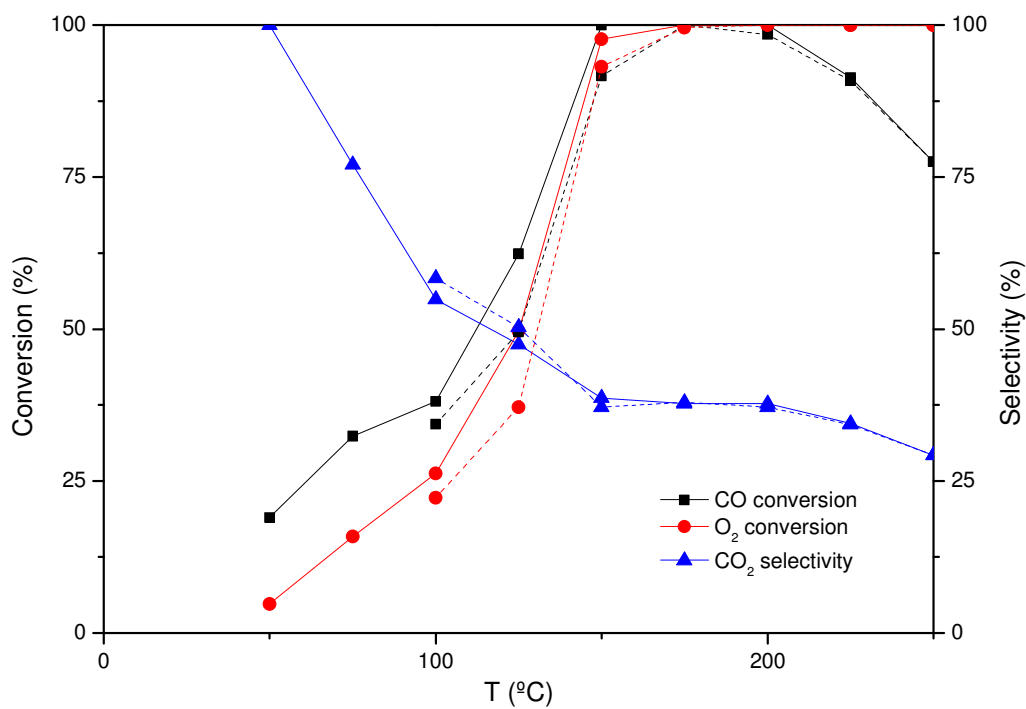
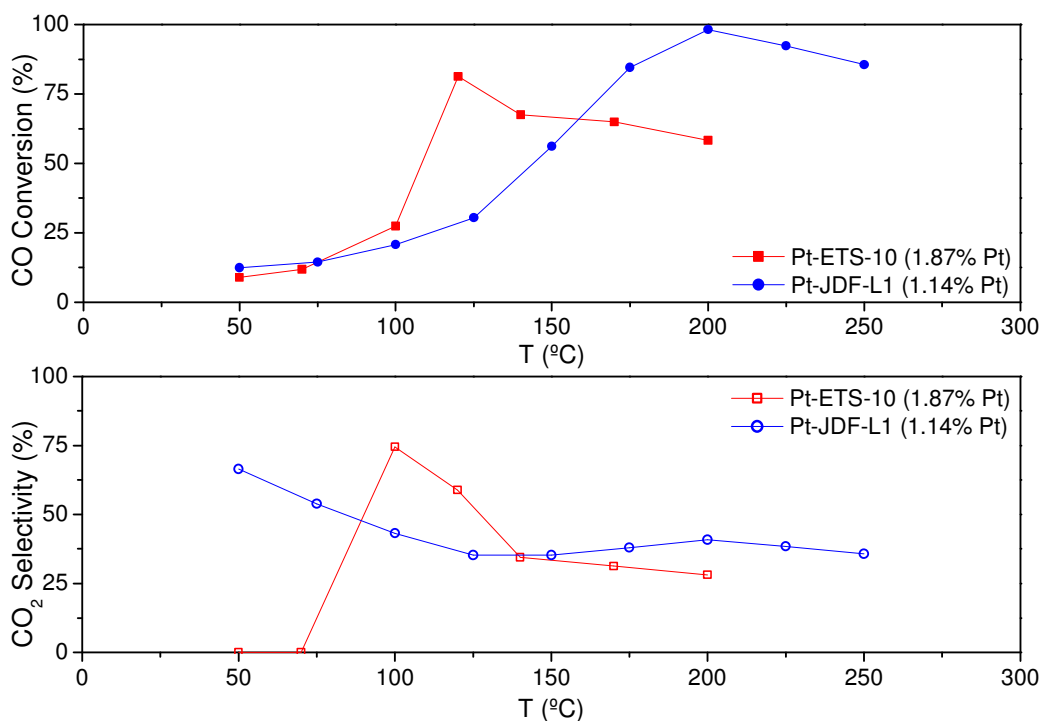


Figure 27.- Pt-JDF-L1 Monolith (5.21% Pt). WHSV = 30 mL/h·mg. Solid lines: increasing temperature. Dashed lines: decreasing temperature.

For the monolith, both conversions and selectivity are quite similar, but for the powder, CO<sub>2</sub> selectivity is not reproducible since higher values are obtained when cooling than upon heating, and subsequently, CO conversion is also affected. Thus, we can conclude that the experiments are not truly reproducible. However, the lack of reproducibility is favourable to us, since the selectivity and CO conversion of the powder are increased. Several consecutive measurements should be performed, with heating measurements again after cooling, if we desire to further assess the reproducibility issue and check if the increased selectivity is maintained while heating.



**Figure 28.- Catalytic performance of Pt-exchanged titanasilicate powders. WHSV = 30 mL/h·mg.**

If we compare the catalytic performances of Pt-ETS-10 and Pt-JDF-L1 (*Figure 28*) we can observe that, despite having a lower Pt content, Pt-JDF-L1 reaches higher CO conversion values than Pt-ETS-10. The ETS-10 catalytic powder we are using for comparison was already available from a previous project by a fellow researcher, but its light-off temperatures are, however, not in agreement with previous results using Pt-ETS-10 with higher Pt loadings (7.3 wt.%) and WHSV of 120 mL/h·mg reported by Sebastian et al.<sup>[13,34]</sup> that showed  $T_{50} = 170$  °C. This Pt-ETS-10 has a much lower Pt content, and though the WHSV is lower, a  $T_{50}$  of 110 °C is a big difference that makes us think that set of data may be unreliable. Those reported light-off values for Pt-ETS-10 ( $T_{50} = 170$  °C;  $T_{75} = 200$  °C)<sup>[13]</sup> when compared to those of our Pt-JDF-L1 powder

( $T_{50} = 144\text{ }^{\circ}\text{C}$ ;  $T_{98} = 200\text{ }^{\circ}\text{C}$ ) still show that JDF-L1 as catalytic support provides better catalytic performance, both in light-off temperatures, that are lower, and in maximum CO conversion values, which are higher. This could be attributed to the larger external surface of JDF-L1 crystals, due to its laminated and open morphology, compared to the small and compact crystals of ETS-10. This morphological advantage causes a higher exposure of Pt particles, granting better accessibility of the reactant gases.

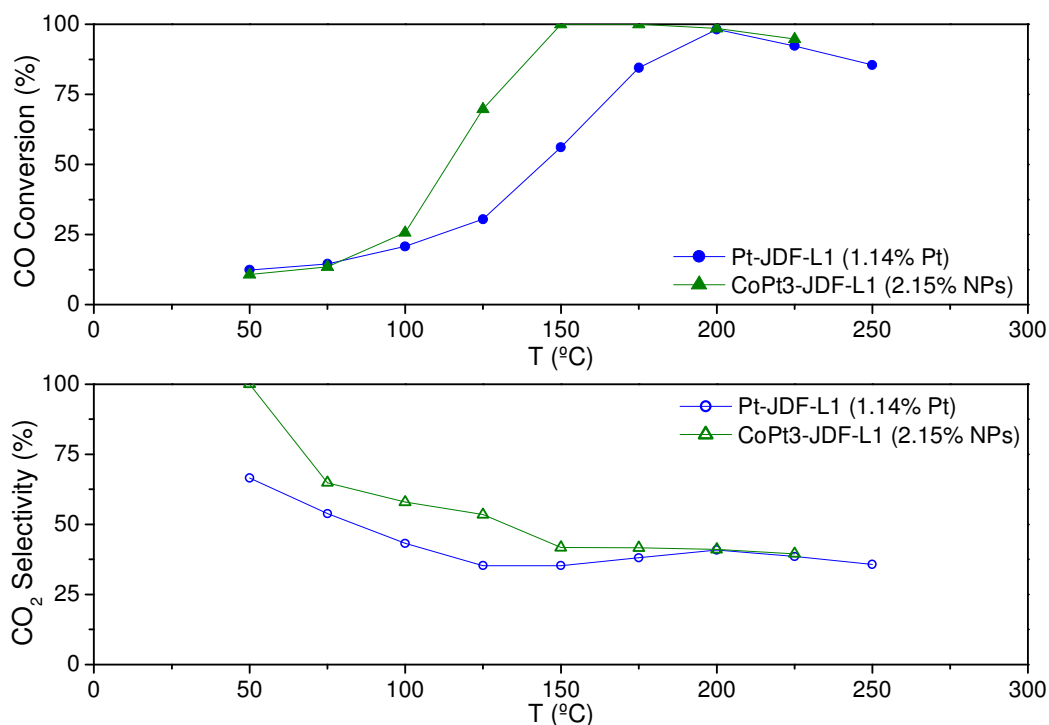


**Figure 29.- Catalytic performance of Pt- and CoPt<sub>3</sub>-JDF-L1 powders. WHSV = 30 mL/h·mg.**

Comparing Pt-JDF-L1 with CoPt<sub>3</sub>-JDF-L1 (Figure 29), we can observe the improved performance of the powder containing cobalt. Light-off temperatures are approximately 50 °C lower for CoPt<sub>3</sub> than for the Pt powder ( $T_{50}=114^{\circ}\text{C}$  and  $T_{100}=150^{\circ}\text{C}$  for CoPt<sub>3</sub>;  $T_{50}=144^{\circ}\text{C}$  and  $T_{98}=200^{\circ}\text{C}$  for Pt). For CoPt<sub>3</sub>, total CO conversion is reached at 150 °C and maintained until 175 °C, when the conversion starts to decay, but slowly. Selectivity is higher overall for the CoPt<sub>3</sub> powder.

This improved performance is, in part, because of the higher metal loading of CoPt<sub>3</sub>-JDF-L1. But it must also be a consequence of the cobalt presence in the sample. High catalytic activities of CoPt<sub>3</sub> catalysts have been reported, and this activity appears to be related to the easier adsorption of oxygen to the particles compared to surfaces of pure Pt, and to the weaker adsorption of CO (due to geographic and electronic effects caused by the Co metal atoms on the particles)<sup>[16,35]</sup>. Our CoPt<sub>3</sub>-JDF-L1 powder results are in

moderate agreement with reported performances of other similar catalysts, like CoPt<sub>3</sub>-SiO<sub>2</sub> (3 wt.% NPs)<sup>[16]</sup> with T<sub>100</sub> = 180 °C using WHSV = 170 mL/h·mg. Our selectivity, however, is much lower.

Pt-JDF-L1, as observed in the TEM images (*Figure A 7*), has plenty of small sized (~2.6 nm) Pt particles well distributed over the crystal surfaces. CoPt<sub>3</sub> nanoparticles of CoPt<sub>3</sub>-JDF-L1, on the other hand, are highly agglomerated and thus the distribution is very heterogeneous, but this does not appear to be detrimental to CO conversion, since the final load of metals is higher. It will be necessary to achieve a more homogeneous NP deposition and evaluate the metal dispersion using chemisorption techniques to reach further conclusions.

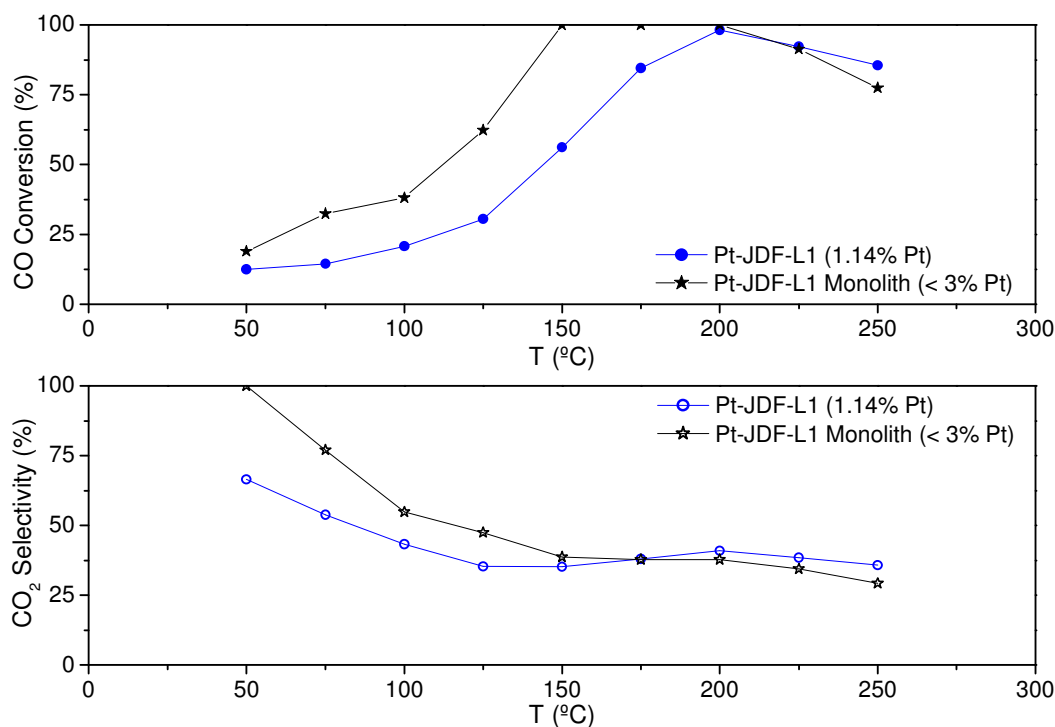


**Figure 30.- Catalytic performance of Pt-JDF-L1 powder vs monolith. WHSV = 30 mL/h·mg.**

A comparison of the Pt-JDF-L1 powder catalytic performance with that of the Pt-JDF-L1 monolith (*Figure 30*) reveals an enhancement of the catalytic activity when changing from fixed bed reactor to structured microreactor. Both experiments were conducted with the same WHSV and measurements taken at the same temperatures for the results to be comparable. Light-off temperatures are ~50 °C lower for the monolith (T<sub>50</sub>=112°C and T<sub>100</sub>=150°C for Pt-monolith; T<sub>50</sub>=144°C and T<sub>98</sub>=200°C for Pt-powder), and once total CO conversion has been reached, it is maintained until 200 °C, the point at which

the powder achieves its maximum conversion. After this point, the monolith conversion and selectivity values drop below those observed for the powder.

The enhanced catalytic performance of the catalyst supported on the monolith can be explained by the higher surface/volume ratio characteristic of structured microreactors, and the straight-channel monolith structures coated with thin-film catalysts are known to enhance diffusion of reactants towards active sites<sup>[35]</sup>. The enhancement is so notable, that the performance of the Pt-JDF-L1 monolith equals and nearly surpasses that of the CoPt<sub>3</sub>-JDF-L1 catalytic powder. However, we also have to take into account the metal loading of the monolith. SEM-EDX analysis of the monolith produced an overestimation of the Pt loading, so we only know that the load of the monolith is 3% or lower. An accurate determination of the monolith Pt content would be needed to assure that all the catalytic enhancement is due to the catalyst being supported on the microreactor, and not because of the Pt loading.

### 5.3.2.-Ethylene epoxidation

The testing of catalytic activity in ethylene epoxidation was performed for different silver-based catalytic powders. Both ETS-10 and JDF-L1 titanosilicates were tested as supports, and silver was deposited by impregnation and ion exchange procedures. Two different compositions of the gas stream were fed to the reactor, one with equal volumes of oxygen and ethylene, the other with excess oxygen (3:1 in volume). All the experiments were performed with **WHSV = 10 mL/h·mg**. The catalytic performances obtained in the experimental setup were very poor, and ethylene conversion was lower than 0.5% for all studied cases and samples. These results are tabulated in the Appendix, *Table A 4*. The ethylene and oxygen conversions (*Equation 9* and *Equation 10*) and ethylene oxide selectivity (*Equation 11*) were defined based on the product output of the reactor, instead of defining them by input and output flows or concentrations (like for *CO SELOX*) because the input/output formulas presented very large errors due to the very low conversions achieved with the catalysts.

For the experiments with a gas feed comprising 6% of O<sub>2</sub> and 6% of C<sub>2</sub>H<sub>4</sub>, only the **Ag-ETS-10 (IWI)** powder achieved ethylene oxide production, though with low selectivity (compared to industry) and almost null ethylene conversion values. At high temperatures the formation of acetaldehyde (AA) was observed in some of the samples, which tells us that the reaction was happening through the OMC intermediate, as explained in the introductory section 3.5.-, which is not the desired pathway. In the

remaining powders, only ethylene combustion was observed. For the experiments with a gas feed comprising 6% of O<sub>2</sub> and 2% of C<sub>2</sub>H<sub>4</sub>, no catalytic activity was observed, only ethylene combustion.

The observed lack of catalytic activity cannot be attributed to the silver loading, since the impregnated Ag-ETS-10 powder showed activity but the similarly loaded impregnated Ag-JDF-L1 did not. The explanation of this result lies in the particle size of the deposited silver. It is widely accepted that for silver, the catalytic effect typical of nanoparticles is observed in the range of 10-100 nm, with <10 nm particles generally considered inactive<sup>[30]</sup>. Good catalytic performance on this wide size range has been explained by different authors as arising from changes in the surface structure or particle morphology and an effect of the support nature has been ruled out. The activity of silver comes from its 100 and 001 planes, more of which are exposed in bigger crystals than in nanoparticles, with cubic shapes also promoting this exposure. The fact that remains is that the rate of ethylene epoxidation is increased 20-fold when changing the silver particle size from 30 nm to 50 nm, and the catalyst activity remains unchanged within the 50-100 nm range, as reported by different studies that also acknowledge the influence of particle shape on the catalyst performance<sup>[30,31]</sup>. Our silver particles are not that large (see *Table 6*), in fact, the silver exchanged powders have an average particle size on the verge of the catalytic range, and the impregnated powders have even smaller particles. However, the powders also have bigger metallic particles (from 20 to 100 nm), though they are much less frequent than the sub-20nm particles. Given all this, no activity would be expected from these powders with such small particles, and the results obtained are in correlation with this. It should not be a surprise either, that the catalytic powder for which the highest number of particles in the catalytic range were observed, Ag-ETS-10 IWI (*Figure A 6*), is the only catalyst that has shown any activity. However, the number of these particles is so low that the activity is almost non-existent.

## 6.-Conclusions and future work

1. Seed deposition and the subsequent titanosilicate crystal layer growth on ceramic monoliths were successfully achieved, with a homogeneous distribution of crystals and layer thicknesses of 18  $\mu\text{m}$ .
2. The crystal phase obtained on the monoliths was JDF-L1 with a layered morphology that enables good accessibility of reactants.
3. In the SELOX catalytic testing, the Pt-JDF-L1 catalytic powder showed good performance ( $T_{50} = 144\text{ }^{\circ}\text{C}$ ;  $T_{98} = 200\text{ }^{\circ}\text{C}$ ), similar to other related catalysts (Pt-ETS-10,  $T_{50} = 170\text{ }^{\circ}\text{C}$ ;  $T_{75} = 200\text{ }^{\circ}\text{C}$ ).
4.  $\text{CoPt}_3$ -JDF-L1 catalytic powders had an increased performance compared to the Pt-exchanged powders, thanks to the beneficial effect of Co on the activity ( $T_{50}=114^{\circ}\text{C}$  and  $T_{100}=150^{\circ}\text{C}$ ).
5. Performance of Pt-JDF-L1 was enhanced when supported in monoliths ( $T_{50}=112^{\circ}\text{C}$  and  $T_{100}=150^{\circ}\text{C}$ ), proving the advantages of structured microreactors.
6. Silver deposition on titanosilicate supports by ion exchange or impregnation yields too small metal particles, out of the catalytic range for silver in ethylene epoxidation.

Future work in this project would involve:

1. Developing a  $\text{CoPt}_3$ -JDF-L1 monolith, in the hopes of obtaining an even higher catalytic performance.
2. Finding new procedures for deposition of silver onto supports that yield bigger particles, inside the catalytic range, or synthesizing specifically shaped silver particles (nanocubes, nanowires) in the catalytic range that combined size and shape effects for an increased performance.

## 7.- References

- [1] - Anderson, J. A.; Fernández García, M. *Supported Metals in Catalysis*; Catalytic Science Series; Imperial College Press: Singapore, 2005; Vol. 5, pp 380.
- [2] - Suppes, G. J.; Dasari, M. A.; Doskocil, E. J.; Mankidy, P. J.; Goff, M. J. Transesterification of soybean oil with zeolite and metal catalysts. *Applied Catalysis A: General* **2004**, *257*, 213-223.
- [3] - Anderson, M. W.; Terasaki, O.; Ohsuna, T.; Philippou, A.; Mackay, S. P.; Ferreira, A.; Rocha, J.; Lidin, S. Structure of the Microporous Titanosilicate Ets-10. *Nature* **1994**, *367*, 347-351.
- [4] - Wang, X.; Jacobson, A. J. Crystal structure of the microporous titanosilicate ETS-10 refined from single crystal X-ray diffraction data. *Chemical Communications* **1999**, 973-974.
- [5] - Lv, L.; Su, F.; Zhao, X. S. A reinforced study on the synthesis of microporous titanosilicate ETS-10. *Microporous and Mesoporous Materials* **2004**, *76*, 113-122.
- [6] - Zhao, G. X. S.; Lee, J. L.; Chia, P. A. Unusual adsorption properties of microporous titanosilicate ETS-10 toward heavy metal lead. *Langmuir* **2003**, *19*, 1977-1979.
- [7] - Philippou, A.; Rocha, J.; Anderson, M. W. The strong basicity of the microporous titanosilicate ETS-10. *Catalysis Letters* **1999**, *57*, 151-153.
- [8] - Roberts, M. A.; Sankar, G.; Thomas, J. M.; Jones, R. H.; Du, H.; Chen, J.; Pang, W.; Xu, R. Synthesis and structure of a layered titanosilicate catalyst with five-coordinate titanium. *Nature* **1996**, *381*, 401-404.
- [9] - Ferdov, S.; Kostov-Kytin, V.; Petrov, O. A rapid method of synthesizing the layered titanosilicate JDF-L1. *Chemical Communications* **2002**, 1786-1787.
- [10] - Rubio Hortells, C. "SÍNTESIS Y APLICACIÓN DE TITANOSILICATOS Y ESTANOSILICATOS LAMINARES Y DESLAMINADOS", Universidad de Zaragoza, Zaragoza, 2012.
- [11] - Avila, P.; Montes, M.; Miró, E. E. Monolithic reactors for environmental applications: A review on preparation technologies. *Chem. Eng. J.* **2005**, *109*, 11-36.
- [12] - Sharaf, O. Z.; Orhan, M. F. An overview of fuel cell technology: Fundamentals and applications. *Renewable and Sustainable Energy Reviews* **2014**, *32*, 810-853.
- [13] - Sebastian, V.; Irusta, S.; Mallada, R.; Santamaria, J. Selective oxidation of CO in the presence of H<sub>2</sub>, CO<sub>2</sub> and H<sub>2</sub>O, on different zeolite-supported Pt catalysts. *Applied Catalysis A-General* **2009**, *366*, 242-251.
- [14] - Park, E. D.; Lee, D.; Lee, H. C. Recent progress in selective CO removal in a H<sub>2</sub>-rich stream. *Catalysis Today* **2009**, *139*, 280-290.
- [15] - Liu, K.; Wang, A.; Zhang, T. Recent advances in preferential oxidation of CO reaction over platinum group metal catalysts. *ACS Catalysis* **2012**, *2*, 1165-1178.
- [16] - Komatsu, T.; Tamura, A. Pt<sub>3</sub>Co and PtCu intermetallic compounds: Promising catalysts for preferential oxidation of CO in excess hydrogen. *Journal of Catalysis* **2008**, *258*, 306-314.
- [17] - Ozbek, M. O.; Onal, I.; Van Santen, R. A. Why silver is the unique catalyst for ethylene epoxidation. *Journal of Catalysis* **2011**, *284*, 230-235.
- [18] - Özbek, M. O.; Van Santen, R. A. The mechanism of ethylene epoxidation catalysis. *Catalysis Letters* **2013**, *143*, 131-141.
- [19] - Rocha, J.; Ferreira, A.; Lin, Z.; Anderson, M. W. Synthesis of microporous titanosilicate ETS-10 from TiCl<sub>3</sub> and TiO<sub>2</sub>: a comprehensive study. *Microporous and Mesoporous Materials* **1998**, *23*, 253-263.
- [20] - Casado, C.; Amghouz, Z.; Garcia, J. R.; Boulahya, K.; Gonzalez-Calbet, J. M.; Tellez, C.; Coronas, J. Synthesis and characterization of microporous titanosilicate ETS-10 obtained with different Ti sources. *Mater. Res. Bull.* **2009**, *44*, 1225-1231.
- [21] - Rubio, C.; Casado, C.; Uriel, S.; Tellez, C.; Coronas, J. Seeded synthesis of layered titanosilicate JDF-L1. *Mater Lett* **2009**, *63*, 113-115.



- [22] - Du, X. Y.; Inokuchi, M.; Toshima, N. Preparation and characterization of Co-Pt bimetallic magnetic nanoparticles. *J Magn Magn Mater* **2006**, *299*, 21-28.
- [23] - Tosheva, L.; Doyle, A. M. Strategies Towards the Assembly of Preformed Zeolite Crystals into Supported Layers. *Ordered Porous Solids* **2009**, 501-519.
- [24] - Mosca, A.; Hedlund, J.; Webley, P. A.; Grahn, M.; Rezaei, F. Structured zeolite NaX coatings on ceramic cordierite monolith supports for PSA applications. *Microporous and Mesoporous Materials* **2010**, *130*, 38-48.
- [25] - Lin, Z.; Rocha, J.; Navajas, A.; Tellez, C.; Coronas, J.; Santamaria, J. Synthesis and characterisation of titanosilicate ETS-10 membranes. *Microporous and Mesoporous Materials* **2004**, *67*, 79-86.
- [26] - Wang, X. Q.; Jacobson, A. J. Crystal structure of the microporous titanosilicate ETS-10 refined from single crystal X-ray diffraction data. *Chemical Communications* **1999**, 973-974.
- [27] - Brill, R.; Hermann, C.; Peters, C. Studien ueber chemische Bindung mittels Fourieranalyse III. Die Bindung im Quarz. *Naturwissenschaften* **1939**, *27*, 676-677.
- [28] - Ferdov, S.; Kolitsch, U.; Lengauer, C.; Tillmanns, E.; Lin, Z.; Sa Ferreira, R. A. Refinement of the layered titanosilicate AM-1 from single-crystal X-ray diffraction data. *Acta Crystallographica Section E-Structure Reports Online* **2007**, *63 (11)*, i186.
- [29] - Galioglu, S.; Zahmakiran, M.; Eren Kalay, Y.; Özkar, S.; Akata, B. Effect of silver encapsulation on the local structure of titanosilicate ETS-10. *Microporous and Mesoporous Materials* **2012**, *159*, 1-8.
- [30] - Goncharova, S. N.; Paukshtis, E. A.; Bal'zhinimaev, B. S. Size effects in ethylene oxidation on silver catalysts. Influence of support and Cs promoter. *Applied Catalysis A, General* **1995**, *126*, 67-84.
- [31] - Christopher, P.; Linic, S. In *In Size and shape specific chemistry of Ag nanoparticles in catalytic ethylene epoxidation*; ACS National Meeting Book of Abstracts; 2011; .
- [32] - Ulla, M. A.; Miro, E.; Mallada, R.; Coronas, J.; Santamaria, J. Preparation of highly accessible mordenite coatings on ceramic monoliths at loadings exceeding 50% by weight. *Chemical Communications* **2004**, 528-529.
- [33] - Gibbs, G. V. The polymorphism of cordierite I: The crystal structure of low cordierite. *American Mineralogist* **1966**, *51*, 1068-1087.
- [34] - Sebastian, V.; Irusta, S.; Mallada, R.; Santamaría, J. Microreactors with Pt/zeolite catalytic films for the selective oxidation of CO in simulated reformer streams. *Catalysis Today* **2009**, *147*, S10-S16.
- [35] - Li, H.; Yu, X.; Tu, S. -.; Yan, J.; Wang, Z. Catalytic performance and characterization of Al<sub>2</sub>O<sub>3</sub> supported Pt-Co catalyst coatings for preferential CO oxidation in a micro-reactor. *Applied Catalysis A: General* **2010**, *387*, 215-223.

# APPENDIX

## MAIN BODY MATERIALS

### LIST OF TABLES

Table 1.- Summary of methods for obtaining small crystals of ETS-10 and JDF-L1 by hydrothermal synthesis. For all methods: pH 10.4; Static crystallization; T=230 °C. ....	11
Table 2.- Main parameters of the different seeding procedures. ....	15
Table 3.- Summary of the different methodologies tested for the growth of a titanosilicate layer onto the monolith supports. For all methods: Gel pH = 10.4... ..	17
Table 4.- Summary of information from the synthesized ETS-10 crystal batches. Crystal sizes were only measured for selected batches. ....	25
Table 5.- Summary of information from the synthesized JDF-L1 crystal batches. ....	28
Table 6.- Summary of prepared catalytic powders and their characteristics. *=Value obtained for the individual NPs in <i>Figure 17</i> . ....	33
Table 7.- Average weight gain of monoliths after ETS-10 seed deposition by different methods. ....	34
Table 8.- Relative weight gain of monoliths after growth by different hydrothermal synthesis methods. Seeding of the monoliths was performed by <i>Sonication (13 wt. %)</i> . ....	37
Table 9.- Average relative gains and average mass of the catalytic support achieved on monoliths after growth for each synthesis method. ....	37
Table 10.- Average chemical composition of an Ag-exchanged monolith by EDX analysis. ....	40
Table 11.- Average chemical composition of a Pt-exchanged monolith by EDX analysis. ....	40

### LIST OF FIGURES

Figure 1.- Projection of the ETS-10 structure down the (100) direction. SiO <sub>4</sub> units are striped or shaded (two types of connections), and TiO <sub>6</sub> units are dotted. ....	3
Figure 2.- JDF-L1 representations made with PowderCell 2.4 from crystallographic data (taken from <sup>[10]</sup> ). Red: O, Blue: Na, Green: Ti, Yellow: Si. (a) structure's view along [100] or the equivalent [010] direction; (b) view along [001] direction. ....	4
Figure 3.- Diagram of preparation pathways for monolithic catalysts <sup>[11]</sup> . ....	5
Figure 5.- Molecular mechanism for ethylene epoxidation through the OMC intermediate. ....	8
Figure 8.- Experimental setup for catalytic activity analysis of SELOX powder and microreactor catalysts. 1- Feed gas cylinders. 2- Mass flow meters ( <i>5850 TR series, Brooks</i> ). 3- Mass flow controller. 4- Valves for operation control. 5- Quartz reactor ( $\phi = 7$ mm for powders or $\phi = 16$ mm for monoliths). 6- Oven with PID Eurotherm temperature controller. 7- Thermocouple with quartz sheath and temperature controller. 8- Bubble-meter for inlet and outlet flow measurement. 9- Gas chromatographer. 10- Computer system and software. 11- Portable CO sensor. ....	18
Figure 9.- Experimental setup for catalytic activity analysis of ethylene epoxidation catalytic powders. 1- Feed gas cylinders. 2- Mass flow meters ( <i>EL-FLOW Select, Bronkhorst</i> ). 3- Mass flow controller. 4- Valves for operation control. 5- Quartz reactor ( $\phi = 7$ mm). 6- Oven with PID Eurotherm temperature controller. 7-	

Thermocouple with temperature controller. 8- Bubble-meter for inlet and outlet flow measurement. 9- Gas chromatographer. 10- Computer system and software.	20
Figure 11.- XRD spectra from simulated ETS-10 <sup>[26]</sup> and from experimental batches B1, B5 and B7. Peaks marked with x correspond to quartz impurities <sup>[27]</sup>	26
Figure 12.- SEM images of ETS-10 crystals from batches B1 (A) and B5 (B), accompanied by the histograms obtained from the particle size distribution analysis.	27
Figure 13.- XRD spectra from simulated JDF-L1 <sup>[28]</sup> and from experimental batches B2 and B3-S. No impurities identified.	28
Figure 14.- SEM images of JDF-L1 crystals. A) JDF-L1 B2; B) JDF-L1 B2-S.	29
Figure 15.- SEM image of JDF-L1 B3-S and its size distribution histogram.	30
Figure 16.- XRD spectra of the CoPt <sub>3</sub> NPs and reference peak locations (from ICDD) for NaCl (red), Pt (grey) and CoPt <sub>3</sub> (blue).	31
Figure 17.- TEM image of CoPt <sub>3</sub> nanoparticles and the particle size distribution histogram.	32
Figure 18.- Zeta potential vs pH representation of the samples. Values of zeta potential in ethanolic solution are shown in the right section of the graph. Tabulated values available in <i>Table A 1</i> .	32
Figure 19.- SEM images of ETS-10 coatings on monoliths deposited by different methods.	35
Figure 20.- SEM image and size distribution histogram of crystals grown by the TiCl <sub>3</sub> -A method.	37
Figure 21.- Transversal SEM image of a monolith titanosilicate layer, with the corresponding size distribution histogram and the average thickness value.	38
Figure 22.- XRD spectrum from Monolith 24's surface compared to JDF-L1 <sup>[28]</sup> and Cordierite <sup>[33]</sup> simulation spectra.	38
Figure 23.- XRD spectrum of the leftover gel from M24's synthesis, compared to JDF-L1 <sup>[28]</sup> and ETS-10 <sup>[26]</sup> simulation spectra.	39
Figure 24.- SEM images of the leftover gel from M24's synthesis.	39
Figure 25.- Metal particles observed on titanosilicate crystals of the ion-exchanged monoliths. Images obtained with a Backscattered electron detector.	41
Figure 26.- Pt-JDF-L1 Powder (1.14% Pt). WHSV = 30 mL/h-mg. Solid lines: increasing temperature. Dashed lines: decreasing temperature.	42
Figure 27.- Pt-JDF-L1 Monolith (5.21% Pt). WHSV = 30 mL/h-mg. Solid lines: increasing temperature. Dashed lines: decreasing temperature.	42
Figure 28.- Catalytic performance of Pt-exchanged titanosilicate powders. WHSV = 30 mL/h-mg.	43
Figure 29.- Catalytic performance of Pt- and CoPt <sub>3</sub> -JDF-L1 powders. WHSV = 30 mL/h-mg.	44
Figure 30.- Catalytic performance of Pt-JDF-L1 powder vs monolith. WHSV = 30 mL/h-mg.	45

## ADDITIONAL MATERIALS (APPENDIX)

### LIST OF TABLES

Table A 1.- Zeta potential and Mobility values for the studied samples. ....	5
Table A 2.- Relative weight gain of each monolith after ETS-10 seed deposition by different methods. ....	8
Table A 3.- Results from SELOX catalyts testing at increasing temperatures. X = Conversion; S = Selectivity. ....	9
Table A 4.- Results from the ethylene epoxidation catalytic powder testing using different gas feeds and temperatures. X = Ethylene Conversion; S = Ethylene Oxide Selectivity.....	9

### LIST OF FIGURES

Figure A 1.- TGA analyses of metal precursors and cationic polymers. ....	3
Figure A 2.- Additional SEM images of ETS-10 B1 crystals. ....	4
Figure A 3.- Additional SEM images of ETS-10 B5 crystals. ....	4
Figure A 4.- SEM images of ETS-10 B7 crystals. ....	4
Figure A 5.- Additional SEM images of JDF-L1 B3-S crystals.....	5
Figure A 6.- TEM images of the silver-based catalytic powders and their corresponding histograms. A) Ag-ETS-10 (IWI); B) Ag-ETS-10 (IE); C) Ag-JDF-L1 (IWI).....	6
Figure A 7.- TEM images of the Pt and Pt-Co-based catalytic powders and their corresponding histograms. A) Pt-JDF-L1; B) CoPt <sub>3</sub> -JDF-L1. ....	7
Figure A 8.- Additional SEM images of titanosilicate crystal layers grown by the TiCl <sub>3</sub> -A method. ....	7
Figure A 9.- SEM images of additional morphologies found on monoliths grown by the TiCl <sub>3</sub> -A method (M24).....	8

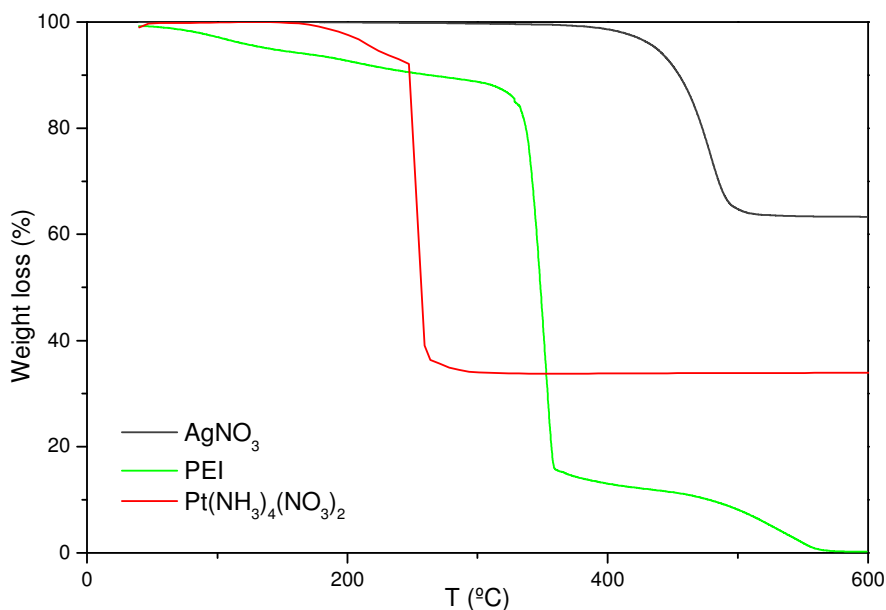
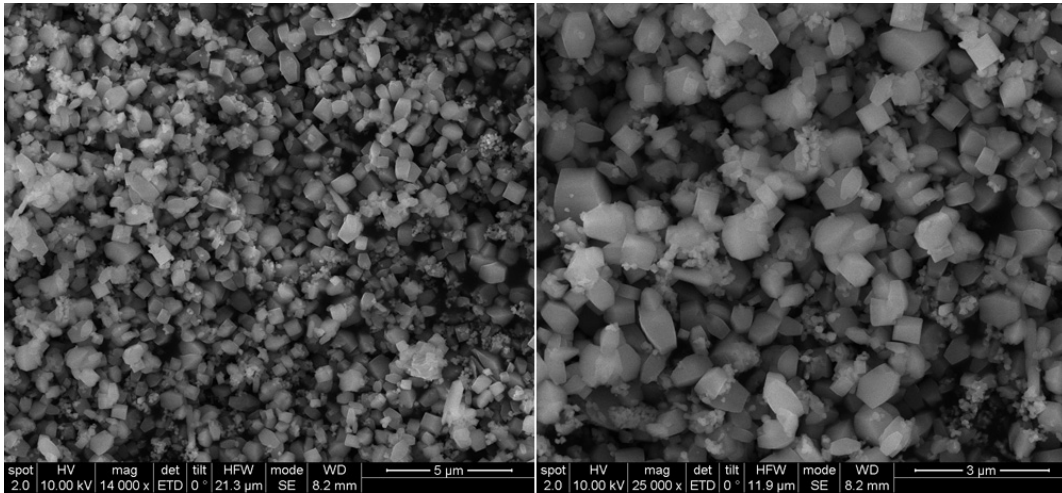
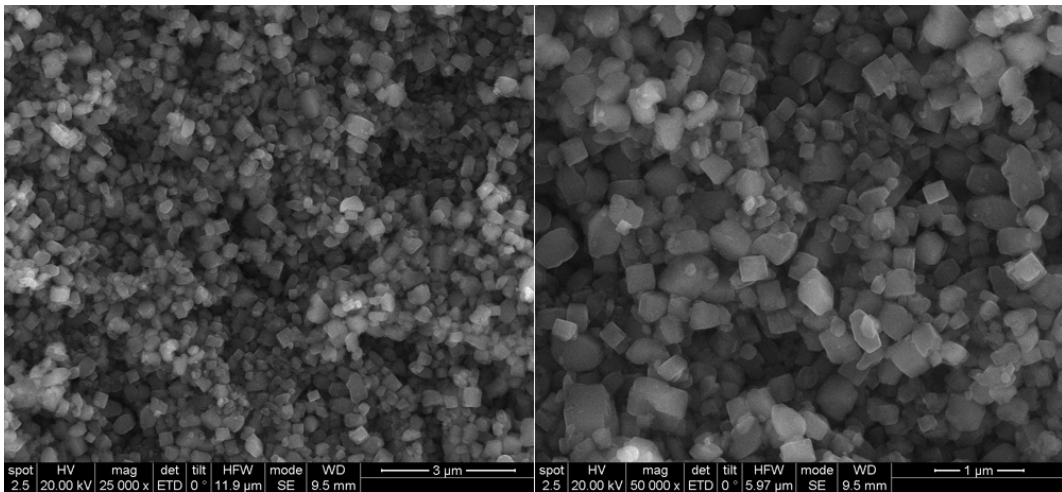


Figure A 1.- TGA analyses of metal precursors and cationic polymers.



**Figure A 2.- Additional SEM images of ETS-10 B1 crystals.**



**Figure A 3.- Additional SEM images of ETS-10 B5 crystals.**

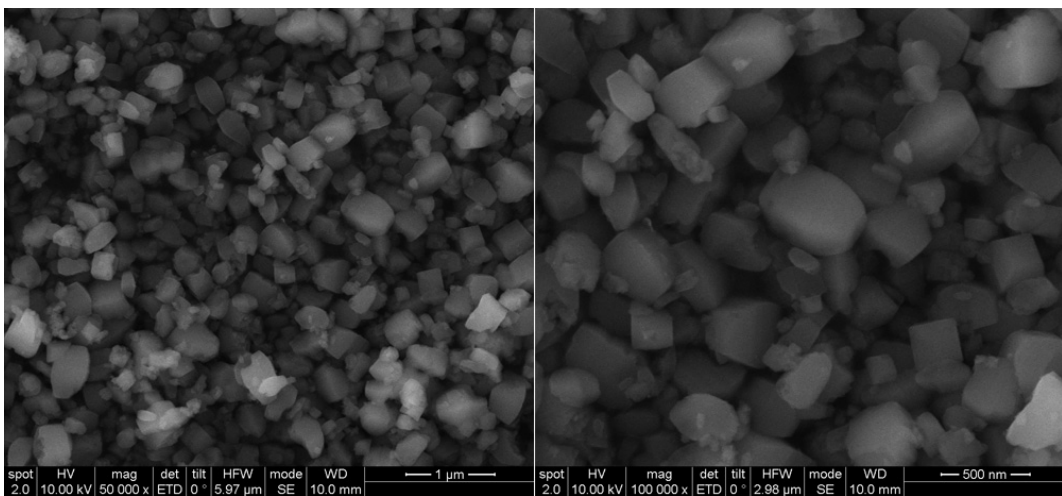


**Figure A 4.- SEM images of ETS-10 B7 crystals.**

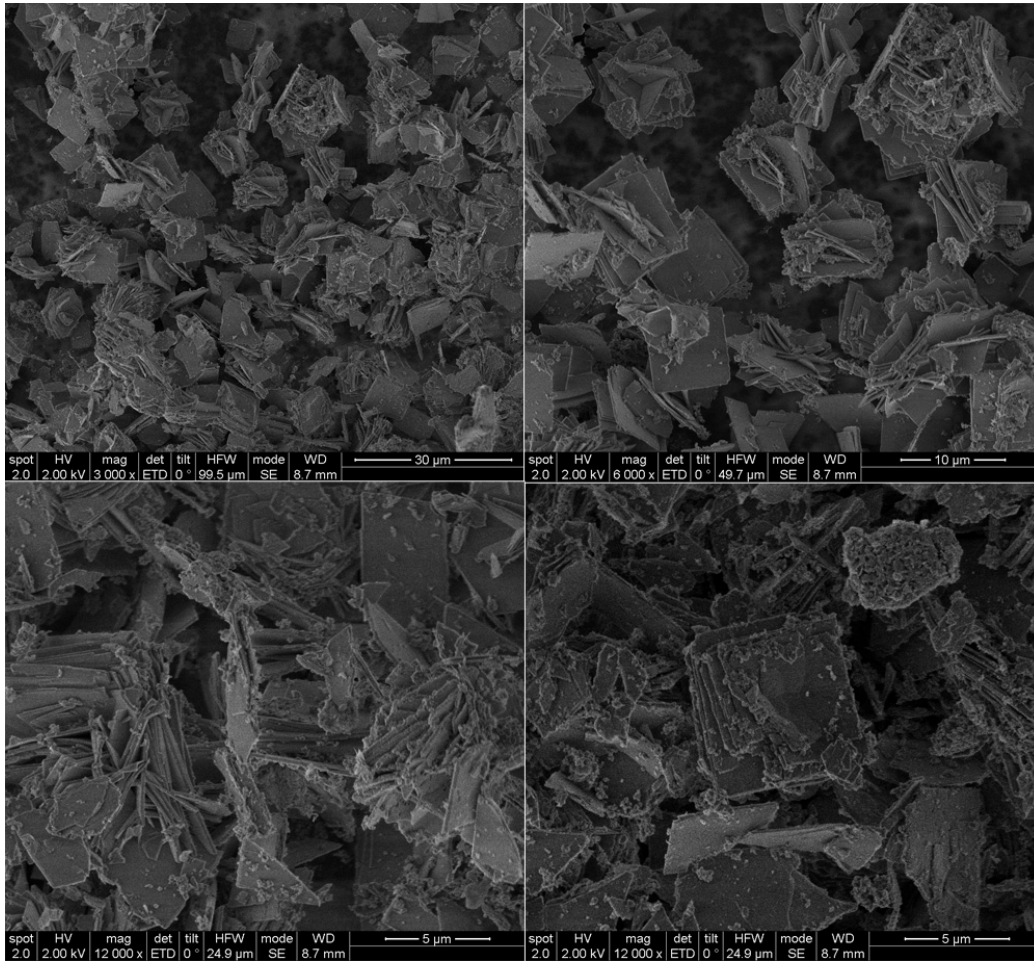
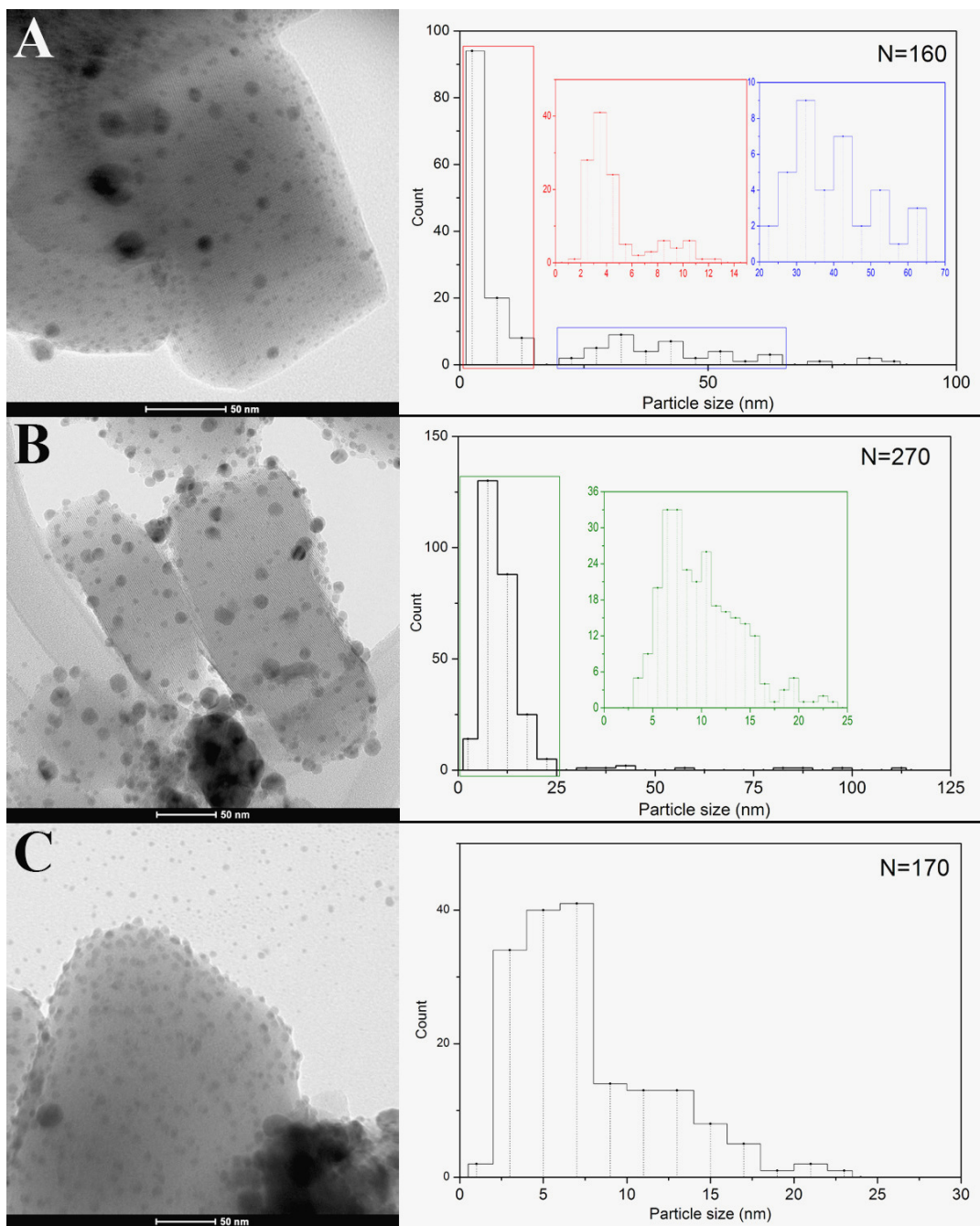


Figure A 5.- Additional SEM images of JDF-L1 B3-S crystals.

Table A 1.- Zeta potential and Mobility values for the studied samples.

Zeta Potential (mV)					
Sample	EtOH	Water			
		pH = 2.5	pH = 5	pH = 8.8	pH = 11
Cordierite	-	7.0 ± 0.1	-30.1 ± 0.6	-31.0 ± 0.6	-42.0 ± 0.8
ETS-10	-22.5 ± 0.2	-42.9 ± 0.8	-47.0 ± 0.9	-47.8 ± 0.9	-49.9 ± 0.9
JDF-L1	-14.7 ± 0.2	-10.2 ± 0.2	-37.2 ± 0.7	-43.6 ± 0.9	-46.6 ± 0.9
CoPt3 NPs	-10.1 ± 0.1	-	-	-	-

Mobility (μm/s)/(V/cm)					
Sample	EtOH	Water			
		pH = 2.5	pH = 5	pH = 8.8	pH = 11
Cordierite	-	0.55 ± 0.01	-2.35 ± 0.04	-2.42 ± 0.04	-3.28 ± 0.06
ETS-10	-0.45 ± 0.00	-3.35 ± 0.06	-3.67 ± 0.07	-3.74 ± 0.07	-3.90 ± 0.07
JDF-L1	-0.29 ± 0.00	-0.80 ± 0.01	-2.91 ± 0.06	-3.41 ± 0.07	-3.64 ± 0.07
CoPt3 NPs	-0.20 ± 0.00	-	-	-	-



**Figure A 6.- TEM images of the silver-based catalytic powders and their corresponding histograms. A) Ag-ETS-10 (IWD); B) Ag-ETS-10 (IE); C) Ag-JDF-L1 (IWI).**

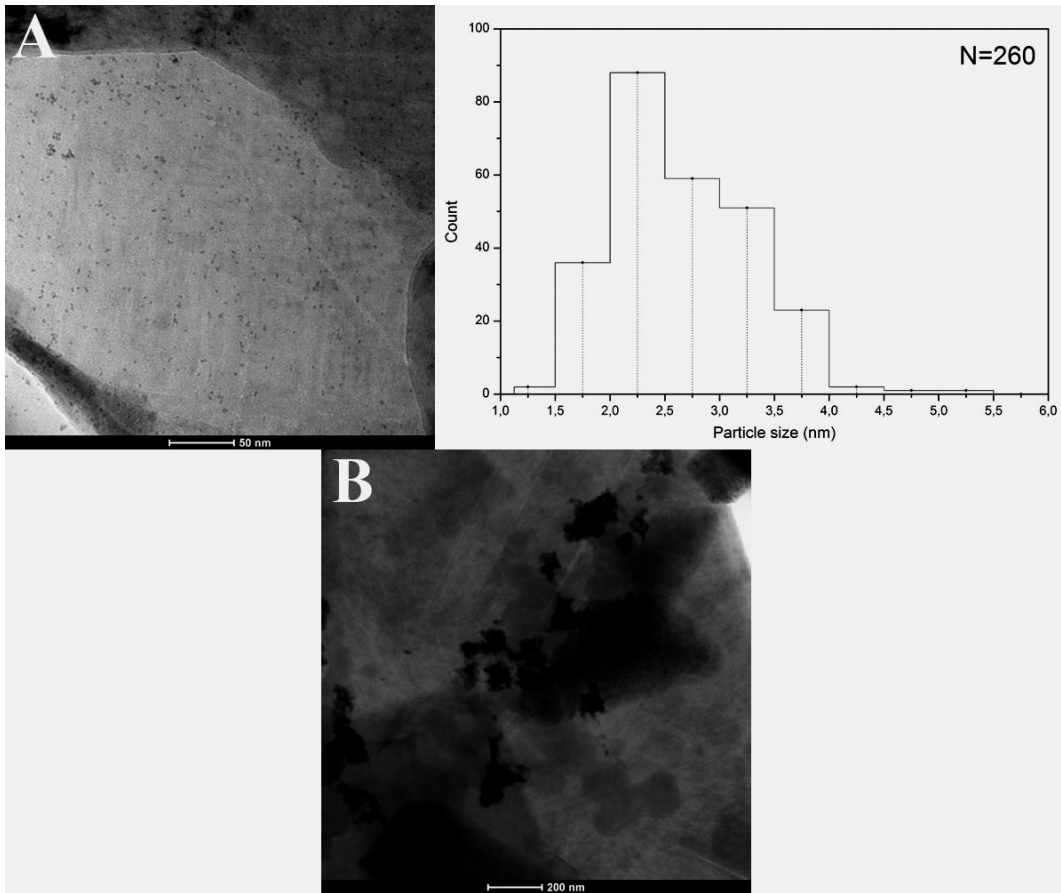


Figure A 7.- TEM images of the Pt and Pt-Co-based catalytic powders and their corresponding histograms. A) Pt-JDF-L1; B) CoPt<sub>3</sub>-JDF-L1.

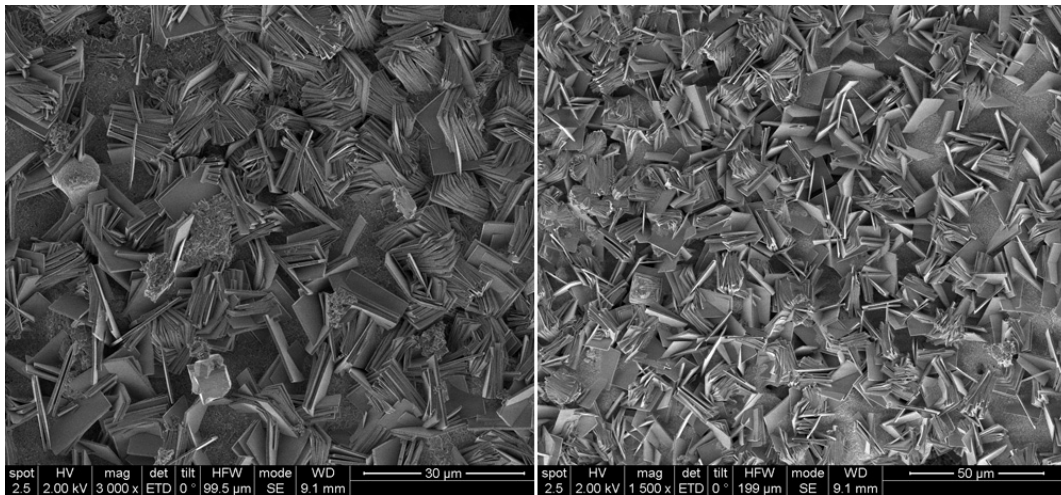


Figure A 8.- Additional SEM images of titanosilicate crystal layers grown by the TiCl<sub>3</sub>-A method.



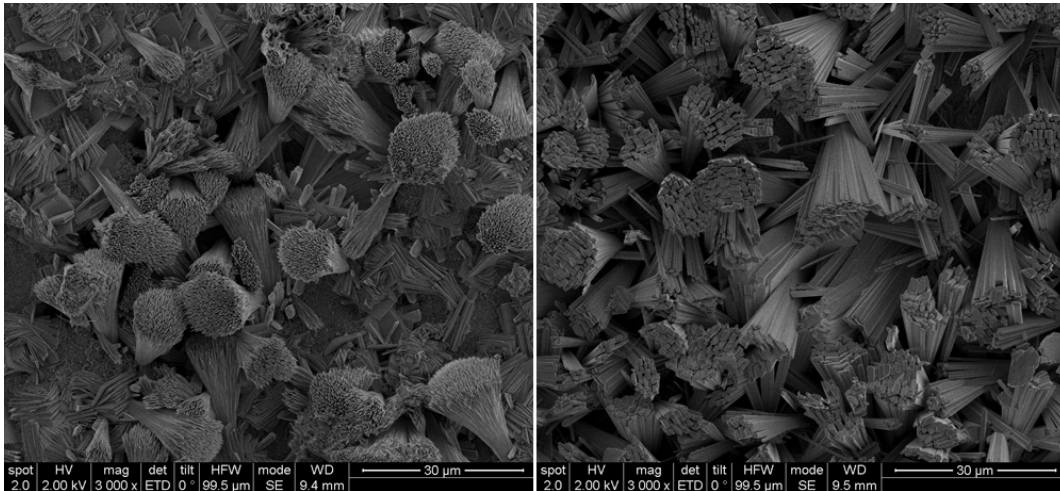


Figure A 9.- SEM images of additional morphologies found on monoliths grown by the  $TiCl_3$ -A method (M24).

Table A 2.- Relative weight gain of each monolith after ETS-10 seed deposition by different methods.

Seeding method	Monolith	Gain <sub>seed</sub> (%)
Sonication	S1M1	3.99
	S1M2	3.16
	S1M3	3.68
	M16	8.49
	M17	9.66
	M18	4.88
	M19	10.08
	M20	9.71
	M21	6.15
	M22	8.63
	M24	9.35
	M25	11.04
	M26	9.06
	M27	8.42
	M28	7.93
	M29	7.67
	M30	8.90
	M31	8.42
	M32	6.75
	M33	6.99
M34	11.25	
M35	9.62	
M36	10.52	
M38	12.08	
M40	8.71	
M41	9.64	

Seeding method	Monolith	Gain <sub>seed</sub> (%)
Sonication*	M5	1.78
	M8	1.48
	M9	3.03
	M10	3.94
	M11	2.29
	M12	6.32
	M13	4.51

Seeding method	Monolith	Gain <sub>seed</sub> (%)
LbL by ES (PEI)	M1	0.79
	M3	1.12
	M6	1.24
LbL by ES (PDDA)	M2	0.46
	M7	0.08

Seeding Method	Monolith	Gain <sub>seed</sub> (%)
Dip Coating	M14	5.88
	M15	8.47

**Table A 3.- Results from SELOX catalysts testing at increasing temperatures. X = Conversion; S = Selectivity.**

<i>T</i> (°C)	<b>Pt-JDF-L1 (1.14% Pt)</b>			<b>CoPt<sub>3</sub>-JDF-L1 (2.15% NPs)</b>			<b>Pt-JDF-L1 Monolith (5.21% Pt)</b>		
	<i>X</i> <sub>CO</sub> (%)	<i>X</i> <sub>O<sub>2</sub></sub> (%)	<i>S</i> <sub>CO<sub>2</sub></sub> (%)	<i>X</i> <sub>CO</sub> (%)	<i>X</i> <sub>O<sub>2</sub></sub> (%)	<i>S</i> <sub>CO<sub>2</sub></sub> (%)	<i>X</i> <sub>CO</sub> (%)	<i>X</i> <sub>O<sub>2</sub></sub> (%)	<i>S</i> <sub>CO<sub>2</sub></sub> (%)
50	12.40	7.75	66.47	10.69	3.56	100.00	18.97	4.78	100.00
75	14.49	11.18	53.81	13.54	8.71	64.84	32.36	15.87	77.03
100	20.75	19.95	43.22	25.68	18.48	57.97	38.09	26.23	54.86
125	30.44	35.85	35.28	69.73	54.47	53.40	62.38	49.64	47.47
150	56.18	66.24	35.24	100.00	100.00	41.69	100.00	97.70	38.67
175	84.53	92.37	38.01	100.00	100.00	41.66	100.00	100.00	37.75
200	98.19	99.81	40.87	98.56	100.00	41.04	100.00	100.00	37.73
225	92.29	99.61	38.49	94.77	100.00	39.46	91.37	100.00	34.46
250	85.54	99.43	35.74	-	-	-	77.50	100.00	29.23

**Table A 4.- Results from the ethylene epoxidation catalytic powder testing using different gas feeds and temperatures. X = Ethylene Conversion; S = Ethylene Oxide Selectivity.**

<i>T</i> (°C)	<i>Catalytic tests with 6% O<sub>2</sub> and 6% C<sub>2</sub>H<sub>4</sub> in the feed.</i>						<i>Catalytic tests with 6% O<sub>2</sub> and 2% C<sub>2</sub>H<sub>4</sub> in the feed</i>			
	<i>Ag-ETS-10 (IWI) (12.72% Ag)</i>		<i>Ag-ETS-10 (IE) (5.86% Ag)</i>		<i>Ag-JDF-L1 (IWI) (13.62% Ag)</i>		<i>Ag-ETS-10 (IWI) (12.72% Ag)</i>		<i>Ag-ETS-10 (IE) (5.86% Ag)</i>	
	<i>X</i> (%)	<i>S</i> (%)	<i>X</i> (%)	<i>S</i> (%)	<i>X</i> (%)	<i>S</i> (%)	<i>X</i> (%)	<i>S</i> (%)	<i>X</i> (%)	<i>S</i> (%)
150	0.01	0.00	0.01	0.00	0.01	0.00	-	-	0.02	0.00
175	0.01	0.00	0.01	0.00	0.01	0.00	0.03	0.00	0.02	0.00
200	0.05	57.09	0.01	0.00	0.01	0.00	0.03	0.00	0.03	0.00
225	0.14	44.50	0.03	0.00	0.02	0.00	0.05	0.00	0.12	0.00
250	0.25	38.18	0.14	0.00	0.41	0.00	0.19	0.00	0.37	0.00
275	0.34	21.77	0.34	0.00	0.41	0.00	0.33	0.00	1.11	0.00
300	0.49	10.50	1.25	0.00	2.11	0.00	0.46	0.00	2.95	0.00